

AD-A171 035

NASA
Contractor Report 175100

USAAVSCOM
Technical Report 86-C-18

Yielding and Deformation Behavior
of the Single Crystal Nickel-Base
Superalloy PWA 1480

Walter W. Milligan, Jr.
Georgia Institute of Technology
Atlanta, Georgia

May 1986

DTIC FILE COPY

Prepared for
Lewis Research Center
Under Grant NAG 3-503

NASA
National Aeronautics and
Space Administration

DISTRIBUTION STATEMENT A

Approved for public release
Distribution Unlimited

DTIC
ELECTE
AUG 1 2 1986
S D



86 8 11 186

TABLE OF CONTENTS

SUMMARY	vi
CHAPTER	
I INTRODUCTION	1
II BACKGROUND	3
Superalloy Microstructures	3
Strength and Deformation	
in High V_f γ/γ' Alloys	4
Temperature Effects	4
Strain Rate Effects	6
Creep Effects	6
Microstructural	
Instability Effects	7
Models of Yielding	7
Brown-Ham Model	8
Ardell Model	9
Huther-Reppich Model	10
Copley-Kear Model	12
Brown-Ham By-Pass Model	14
Temperature Effects	15
Mismatch Effects	15
III EXPERIMENTAL PROCEDURES	17
Material	17
Mechanical Testing	17
Microstructural Evaluation	19
Metallography	19
TEM	19
Dislocation Analysis	21
IV RESULTS AND DISCUSSION	22
Heat Treated Microstructure	22

Mechanical Behavior	23
Temperature Effects	23
Strain Rate Effects	24
Data Correlation	24
Deformation Substructures	25
Low Temperatures	26
High Temperatures	27
Intermediate Temperatures	31
Modeling of the Yield Process	32
Low Temperatures	32
High Temperatures	36
Micro-Mechanics of Yielding	39
V SUMMARY AND CONCLUSIONS	41
Mechanical Behavior	41
Dominant Deformation Mechanisms	42
Detailed Substructures	42
Modeling of Yielding	43
REFERENCES	45
APPENDIX A - DETERMINATION OF CRYSTAL ORIENTATION IN THE TEM	52
APPENDIX B - DISLOCATION AND STACKING FAULT ANALYSIS	57
APPENDIX C - CALCULATION OF CRITICAL STRESSES IN THE HUTHER-REPPICH MODEL	64
APPENDIX D - CALCULATION OF THE TRUE ACTIVATION ENERGY FOR YIELDING	66
TABLES	70
FIGURES	72

SUMMARY

Interrupted tensile tests were conducted to fixed plastic strain levels in on $\langle 001 \rangle$ oriented single crystals of the nickel-base superalloy PWA 1480. Testing was done in the range from 20-1093°C, at strain rates of 0.5 and 50%/min. The yield strength was constant from 20 to 760°C, above which the strength dropped rapidly and became a strong function of strain rate. The high temperature data could be represented very well by an Arrhenius-type equation, which resulted in three distinct temperature regimes. The deformation substructures could also be grouped in the same three regimes, indicating that there was a fundamental relationship between the deformation mechanisms and the activation energies. At low temperatures, the activation energy for yielding was zero, and deformation was dominated by γ' shearing by pairs of $\{111\}_a/2\langle 110 \rangle$ dislocations. At high temperatures, the true activation energy for yielding was calculated to be 500kJ/mol, which is indicative of a diffusion-controlled process, and deformation was dominated by γ' by-pass. Intermediate temperatures exhibited transitional behavior. No currently available precipitation hardening model could adequately describe the behavior observed in



A-1	
by Codes	
and/or	
Special	

the low temperature regime, due to the observation that penetration into the precipitate was not rate-limiting at all temperatures. In the high temperature regime, the functional form of the Brown-Ham by-pass model fit the data fairly well. The results of this study also demonstrated that the initial deformation mechanism was frequently different from that which would be inferred by examination of specimens which had been tested to failure.

CHAPTER I

INTRODUCTION

Nickel-base superalloys are used extensively in applications where high strength and oxidation resistance are required at high temperatures [1]. Recent advances in casting techniques have allowed the development of single crystal components for use in gas turbine engines [2,3]. Due to the lack of grain boundaries in these components, they exhibit superior creep, oxidation, and fatigue resistance over conventionally cast alloys. PWA 1480 is a modern single crystal alloy which is being used as the turbine blade material in advanced aircraft gas turbines [3], and is being considered as the turbopump blade material in the Space Shuttle Main Engine (SSME) [4].

The objective of this research was to characterize the strength and monotonic deformation mechanisms of PWA 1480 as a function of temperature, strain level, and strain rate. This work will serve as a basis for the remainder of the program, which involves studying the cyclic and non-isothermal cyclic deformation behavior of the alloy, and the subsequent development of physically-based constitutive models.

In addition to the goal of characterizing the alloy as a part of the NASA SSME program, a further goal was to add to the fundamental knowledge of deformation processes and yielding behavior in high volume fraction γ/γ' alloys.

CHAPTER II

BACKGROUND

Superalloy Microstructures

Nickel-base superalloys are strengthened by the precipitation of the ordered γ' phase, which has the $L1_2$ structure and is based on $Ni_3(Al,Ti)$. By varying the chemistry and thermomechanical treatment, the composition, volume fraction (V_f), shape, and properties of the γ' can be altered significantly, all of which have major effects on the properties of the superalloy. Several excellent reviews of these topics are available [5,6].

The specific class of superalloys which is of interest to this study contains alloys which have a high V_f of γ' , typically 45-60%. These alloys have excellent strength at high temperatures, and are used at temperatures as high as 1100°C . Mar-M 200 is representative of this class of alloys, and its microstructure has been well documented [7]. The alloy contains about 60 v/o γ' , which is present as a very fine dispersion of cuboidal precipitates. The γ' size depends on the heat treatment, but typical particle diameters are 0.1 to $1.0\ \mu\text{m}$. The alloy also contains MC and $M_{23}C_6$ carbides, eutectic γ/γ' pools, and micropores. Dendritic segregation is

significant in the as-cast condition, but it is reduced substantially by a high temperature homogenizing and solutionizing heat treatment.

Strength and Deformation in

High V_f γ/γ' Superalloys

The following sections present a brief discussion of the strength and deformation behavior of high V_f alloys. A more thorough treatment of strengthening mechanisms and models of yielding appears later in this chapter.

Temperature Effects

The yield strength of these alloys is about constant from 20-750°C [7-12]. The constant strength is the result of the drastic increase in the strength of the γ' precipitates in this temperature regime [13,14]. In this range of temperatures and volume fractions, deformation occurs by shearing of the γ' precipitates by pairs of $a/2\langle 110 \rangle$ dislocations on $\{111\}$ planes. The dislocations travel in pairs in order to minimize the area of the high energy anti-phase boundary (APB) which is created by the $a/2\langle 110 \rangle$ displacement of the superlattice [15]. The high energy of the $\{111\}a/2\langle 110 \rangle$ APB is also responsible for the anomalous strength increase of the γ' : It has been demonstrated [13,14,16] that the reason for the strength increase in pure γ' with temperature is the increased frequency of cross-slip to $\{001\}$ (cube) planes, which is

driven by the vastly lower APB energy (APBE) of the $\{001\}a/2\langle 110 \rangle$ displacement relative to the $\{111\}a/2\langle 110 \rangle$ displacement.

The temperature above which the critical resolved shear stress (CRSS) begins to drop is a function of stress axis orientation [9,10]. This has been shown to be due to the high $\{111\}a/2\langle 110 \rangle$ APBE also: For stress axes which deviate from $\langle 001 \rangle$, the CRSS is sometimes reduced at intermediate temperatures by the occurrence of primary slip on cube planes [9,10].

The reason for the drop in strength above 750°C is not clear in all cases, because the deformation substructures at the yield point have not been well documented, and because the mechanisms of deformation are alloy-specific. Due to the effects of thermal activation, deformation at high temperatures can occur by particle by-pass as well as by particle shearing [17]. By-pass is favored in alloys with a high γ/γ' lattice parameter mismatch, high APBE, and high V_f , while shearing is favored in alloys with a low mismatch, low APBE, and low V_f [17-19]. The tendency to shear is also affected by the matrix stacking fault energy (SFE) and strain rate [17-19]. Whether the γ' is sheared or by-passed, deformation substructures at high temperatures are non-planar and very homogeneous, due to the effects of easy cross-slip, climb, and slip on multiple systems [19].

Strain Rate Effects

In general, strain rate does not affect strength or deformation modes until about 750°C [19,20]. Above 750°C, deformation is thermally activated, and so reductions in the strain rate tend to reduce the flow stress. The strain rate also affects the deformation mode: High strain rates tend to cause planar, inhomogeneous substructures, while lower strain rates tend to cause wavy, homogeneous substructures [19].

Creep Effects

Creep testing or tensile testing at very low strain rates can lead to deformation mechanisms which are not otherwise observed. At intermediate temperatures (700 - 800°C), shearing of the γ' can occur by the $\{111\}\langle 112 \rangle$ system [21-25]. This results in the formation of relatively low energy stacking faults instead of APB's, and can result in large primary creep strains in some orientations [22,25]. This deformation mechanism is usually very heterogeneous, and exhibits a large degree of orientation-dependent behavior.

At higher temperatures (above about 850°C), deformation during creep is much homogeneous, resulting in a much smaller degree of orientation-dependent behavior [9,26]. The same factors which affect yield strength also affect the creep strength [26-30], and the stress level affects the deformation mechanism: Higher stresses tend to

result in more γ' cutting than lower stresses [29].

Microstructural Instability Effects

It has been shown that "hyperfine" γ' can precipitate upon quenching from the ageing temperature in some alloys [31]. When these alloys are subsequently tested at elevated temperatures, some of the "hyperfine" γ' redissolves. The result of this is a varying microstructure as the temperature is raised, which can become the dominant factor in the strength/temperature relationship in some alloys.

Another type of microstructural change takes place in some alloys when they are annealed under stress or creep tested at high temperatures. The γ' can coarsen directionally [32], resulting in a lamellar γ' structure which has excellent longitudinal creep resistance [33-35].

Models of Yielding

It is desirable to develop micro-mechanical models of the yielding process as an aid in the understanding of yielding, and as a guide to alloy development and heat treatment. The theory of yielding for low V_f , underaged superalloys is well developed [36-41]. The model of Brown and Ham is representative, and is briefly described below.

Brown-Ham Model

The Brown-Ham model [37] is based on the observation that dislocations shear the γ' by travelling in "loosely coupled" pairs in low V_f alloys. This means that the dislocations are paired, but are seldom within the same particle. The first dislocation creates APB as it shears the precipitates, so there is a resisting force which causes the dislocation to become locally bent and conform to the particle shape. The second dislocation has the same Burgers vector, so it removes the APB, and its motion is assisted. This causes the second dislocation to remain straight. A static force balance is set up, considering the applied stress, the APB forces, and the elastic interaction forces between the two dislocations. It is assumed that the mismatch force is negligible. The resulting equation for the increase in the CRSS due to precipitates under shearing conditions is

$$\Delta\tau_c = (\gamma_o/2b) [(4\gamma_o r_s f/\pi T)^{1/2} - f] , \quad (2-1)$$

where $fT\pi/4\gamma_o \leq r_s \leq T/\gamma_o$

and

- τ_c = CRSS,
- γ_o = APBE,
- b = Dislocation Burgers vector,
- r_s = Particle radius in slip plane,

$$f = V_f,$$

$$T = \text{Dislocation line tension.}$$

It is clear that the strength is very dependent on APBE, V_f , and particle size. Above a critical particle size, the looping stress can become smaller than the shearing stress, and then the CRSS can be estimated as the Orowan stress,

$$\Delta\tau_c = Gb/L, \quad (2-2)$$

where $G = \text{Shear Modulus,}$
 $L = \text{Particle Spacing.}$

The model has been successfully applied to a number of low V_f alloys [36-41].

Due to the fundamental assumptions that the precipitates may be treated as widely-spaced point obstacles and that the dislocations are weakly coupled, the Brown-Ham model cannot be applied to high V_f , large particle size alloys. Few models are available for these systems, due to the complexity of the dislocation-particle interactions. The models which are available are now considered.

Ardell Model

In their study of an alloy containing 35 v/o γ' , Ardell et. al. [42] noted that the Brown-Ham type models

could not describe the observed yielding behavior. They rederived the Brown-Ham model, eliminating all steps which assumed that the volume fraction was much less than 1. For large particles that are sheared, they obtained the following equation for the CRSS:

$$\Delta\tau_c = (\gamma_o/2b) u , \quad (2-3)$$

where

$$u = \{-B + (B^2/3 + 4B)^{1/2}\} / \{2(1 - B/6)\} , \quad (2-4)$$

and

$$B = 3\pi^2 \gamma_o^2 f r_s / 32T . \quad (2-5)$$

Equation (2-3) is in excellent agreement with their experimental results, but the authors even agree that the model is not theoretically justified. The Brown-Ham derivation assumes that the γ' distribution is described by Fleischer-Friedel statistics, implying a dilute array of point obstacles [43-44]. In addition to this discrepancy, they also proposed that mismatch strengthening may not have been negligible in the peak-aged condition.

Huther-Reppich Model

Huther and Reppich [45-47] have developed a model for high V_f alloys which attempts to overcome both of the serious limitations of the Brown-Ham type models. First, it is not based exclusively on Fleischer-Friedel

statistics, and second, it allows for a transition from "weak" dislocation pair coupling to "strong" dislocation pair coupling above a critical particle size.

The model was derived from the solid solution strengthening theory of Schwarz and Labusch [44], which treats both dilute and concentrated arrays of obstacles. The relationship between the CRSS and the particle size is divided into three regimes, Figure 1. At very small particle sizes, the model predicts that the Brown-Ham theory is valid, and Equation (2-1) will predict the CRSS. Above a critical particle size, "strong" pair coupling will become dominant, and the Brown-Ham theory will break down. The critical particle size can be calculated by

$$d_c = 0.78 w (2T/\gamma_0) , \quad (2-6)$$

where d_c = Critical particle diameter,
 w = Term based on elastic interaction of the paired dislocations; magnitude is on the order of 1.

In this regime, the model predicts a hyperbolic decrease in the cutting stress as a function of particle size:

$$\Delta \tau_c = 0.86 \{Tf^{1/2} w/bd\} \{1.28d\gamma_0/wT - 1\}^{1/2} . \quad (2-7)$$

It should be noted that the model predicts a peak strength which is attributed to a change in the shearing mechanism, not a change from shearing to looping.

At very large particle sizes, the stress necessary to cause the first dislocation to penetrate the particle can become larger than the CRSS calculated in Equation (2-7), and thus dominate the CRSS. The penetration stress is given by

$$\Delta\tau_c = (\gamma_o/b) - (T/br_s) . \quad (2-8)$$

In this regime, the CRSS is a hyperbolically increasing function of particle size, so the model predicts that Orowan by-pass will become competitive with shearing.

The Huther-Reppich model has been subjected to a limited amount of experimental verification, and the results agree fairly well with the theoretical predictions [47-49].

Copley-Kear Model

Copley and Kear [11] have developed two models specifically for alloys such as Mar-M 200. By TEM observations and a computer simulation, they determined that penetration of the first dislocation into the particle was the rate-limiting step during yielding. Their first model is dynamic, and is based on the Gilman dislocation

velocity function. However, in the development of the model they assumed arbitrary values of dislocation velocities in the matrix and the γ' , which pre-determines the final solution. Their second model, which is based on a static force balance and is more fundamentally sound, is now described.

The precipitates are assumed to be spheres, and the mismatch is assumed to be negligible. The critical step is assumed to be the penetration of the first dislocation into the precipitate. At that point, the first dislocation is in the interface, while the second dislocation is in the matrix. The following forces are considered: The applied stress, APB forces, Peierls forces, line tension forces, and the dislocation elastic interaction forces. The force balance results in the following expression for the CRSS:

$$\tau_c = (\gamma_o/2b) - (T/br_s) + 1/2(\tau_m + \tau_p) , \quad (2-9)$$

where τ_m = The CRSS of the matrix,
 τ_p = The CRSS of the γ' precipitates.

Substituting typical values for Mar-M 200 results in a very reasonable value for the CRSS. The force due to the APB term $(\gamma_o/2b)$ accounts for about 80% of the CRSS at room temperature.

Brown-Ham (By-Pass) Model

At high temperatures, precipitate by-pass by dislocations is aided by climb and cross slip [50]. This mechanism can become competitive with shearing at high temperatures and low strain rates. Shewfelt and Brown [51] have developed a model for this phenomenon for a system of spherical particles, and Brown and Ham [37] have developed a similar model for a system of cuboidal particles. The Brown-Ham model will be described here, due to the cuboidal nature of the γ' in the alloys of interest.

When a dislocation approaches an obstacle in its slip plane, it may leave its slip plane by climb, thereby avoiding the obstacle. It is assumed that climb is the rate-limiting step in the process. When a dislocation climbs, vacancies must be emitted or absorbed. For this reason, the climb rate is limited by the diffusion rate of vacancies in the alloy. A thermodynamic calculation of the vacancy flux in the vicinity of the climbing edge dislocation yields the climb rate, and this is used to calculate the CRSS. For a system of cuboidal particles, the CRSS is

$$\tau_c = (Gb/2^{1/2}L) + (dQ_d/2^{1/2}Lb^3) + \\ + (dkT/2^{1/2}Lb^3) \ln (\xi d^2/2\rho b^4 v_o) , \quad (2-9)$$

where Q_d = Activation energy of the rate-limiting
diffusion process,
 k = Boltzmann's constant,
 T = Temperature ($^{\circ}K$),
 $\dot{\epsilon}$ = Strain rate,
 ρ = Mobile dislocation density,
 ν_0 = Debye frequency.

Since the logarithmic term is always negative, the model predicts a linearly decreasing CRSS as a function of temperature. The first term ($Gb/2^{1/2}L$) is a "threshold stress", which is due to the force necessary to increase the dislocation line length during climb.

Temperature Effects

In general, all the models discussed are capable of predicting the temperature dependence of the CRSS through the temperature dependent terms (γ_0 , G , etc). However, the effects of thermal activation on dislocation/particle interactions are not considered in any of the shearing models. Also, care must be taken to insure that the rate-limiting step during deformation does not change when the temperature changes when applying these models.

Mismatch Effects

The effect of the γ/γ' lattice parameter mismatch was not considered in any of the models discussed in this chapter. It has been shown [52-57] that the mismatch may

be an important variable in some alloys, so it should be determined that the mismatch may be ignored before applying any of these models.

CHAPTER III

EXPERIMENTAL PROCEDURES

Material

The composition of the alloy is given in Table 1. Single crystal bars approximately 15 cm in length and 2.5 cm in diameter were produced by TRW, Inc. The crystal orientations were determined by the Laue back-reflection X-ray technique, and all bars whose tensile axes were within 10° of $\langle 001 \rangle$ were accepted. TRW also performed the heat treatment, which consisted of the following steps:

Solutionize @ 1285°C for 4 hrs, rapidly cool;

Age @ 1080°C for 4 hrs, rapidly cool;

Age @ 870°C for 32 hrs, air cool.

Each bar was cut in half and machined, yielding two specimens. The specimens were designed and machined in accordance with ASTM Specification E-8. The specimens were cylindrical, with a 6 mm diameter and a 25 mm gage length.

Mechanical Testing

Interrupted tests were conducted to fixed plastic strain levels in order to study deformation mechanisms which operate during yielding. Tests were conducted at 20,

705, 760, 815, 871, 982, and 1093°C. In order to further study the effects of thermal activation, tests were conducted at two strain rates: 0.5 and 50%/min.

The specimens were induction heated. Three chromel/alumel thermocouples were welded to the specimen surface, one at each end of the gage length and one in the center. A temperature gradient of no more than $\pm 2^\circ\text{C}$ was maintained over the gage length.

Strain was measured by a calibrated high temperature extensometer. The extensometer consisted of a set of alumina probes which were attached to an MTS clip-on gage. The tests were conducted in strain control, using a SATEC computerized testing system. The plastic strain was calculated in real time by the following equation:

$$\epsilon_p = \epsilon_t - \sigma/E , \quad (3-1)$$

where ϵ_p = Plastic strain (Calculated in real time),
E = Elastic modulus (Measured prior to test),
 σ = Stress (Measured in real time),
 ϵ_t = Total strain (Measured in real time).

After the pre-programmed plastic strain was reached, the computer switched to load control and returned the specimen to zero load. The specimen was then immediately cooled to room temperature.

Samples of the same alloy with a slightly higher Al and Ti content which were tested to failure were supplied by Pratt & Whitney Aircraft. These tests were conducted at 760, 871, 982, and 1093°C, and at a strain rate of 0.5%/min. In addition, two samples that had been tested under creep conditions were supplied by P&W. One sample was tested at 871°C and 414 MPa, while the other was tested at 1093°C and 117 MPa.

Microstructural Evaluation

Metallography

Samples were sectioned mounted, polished, and etched for microstructural quantification. The etchant consisted of 33% nitric acid, 33% acetic acid, 33% distilled water, and 1% hydrofluoric acid. Photomicrographs were taken on a Leitz metallograph and a Cambridge S-4 scanning electron microscope (SEM).

The volume fraction of porosity and γ/γ' eutectic constituent were determined by a point counting method [58]. The volume fraction of primary γ' was determined by measuring the average cube-edge length and linear particle density, then modeling the microstructure as an array of ideal cubes.

Transmission Electron Microscopy (TEM)

Thin foils were prepared for TEM from the as-heat treated material and from the tested specimens. Foil

blanks were prepared by slicing 0.4 mm thick wafers with a high-speed sectioning wheel, then grinding the blanks to 0.2 mm thick with 600 grit SiC paper, and finally punching 3 mm diameter disks from the blanks. It was determined that the sample preparation did not deform the material as long as the punch tip was well sharpened.

Foils were prepared by electropolishing the discs in a Struers Tenupol unit. The material proved to be unusually sensitive to electropolishing temperature and voltage, and best results were obtained when fresh solution was used. The following conditions were found to be optimal:

Solution: 5% perchloric acid, 35% butyl
cellusolve, 60% methanol.
Temperature: $-25^{\circ}\text{C} \pm 1^{\circ}\text{C}$.
Voltage: 8.5 - 9.7 V (With 2 mm diameter
holder).

Best results were obtained in voltage control. As shown in Figure 2, the γ' was attacked when the voltage was too low, while the matrix was attacked when the voltage was too high. Also, the optimal voltage changed as the solution was used (correct voltage increased).

Foils were studied with a JEOL 100C microscope operating at 100 kV. Appendix A describes the methods used for determination of crystal directions and orientations. A two-axis tilting stage was used to facilitate crystal

manipulation and diffraction experiments.

Dislocation Analysis

Dislocation Burgers vectors, character, and slip planes were determined after testing to characterize the operative deformation mechanism at each testing condition. Appendix B describes these procedures in detail.

CHAPTER IV

RESULTS AND DISCUSSION

Heat Treated Microstructure

The microstructure of the alloy is similar to that of other high γ' volume fraction alloys typified by Mar-M 200 [7]. The alloy contains a fine dispersion of ordered, cuboidal γ' particles in a disordered γ matrix, Figure 3(a). The γ' size was fairly uniform, ranging from 0.25 to 1.0 μm , with an average size of 0.5 μm . There were isolated areas in the interdendritic regions which contained larger primary γ' particles. In these regions, the average γ' size was about 1 μm , and particles up to 1.5 μm were sometimes observed. No "hyperfine" γ' was found. The primary γ' volume fraction was measured to be 55 - 60%.

As shown in Figure 3(b), the alloy contained a residual dendritic structure with micropores and large interdendritic eutectic pools. The volume fraction of microporosity was measured to be 0.15 - 0.20%. Most pores were spherical, with a diameter of less than 50 μm , but several elongated pores with a major axis length of up to 250 μm were present. The volume fraction of eutectic was measured to be 4.5 - 5.0%. The maximum eutectic pool size

was about 250 μm .

Due to a low carbon content (42 ppm), few carbides were present. The carbides were only occasionally observed via TEM in thin foils, and the maximum observed carbide size was 0.5 μm . No phases other than γ , γ' , and carbides were found.

As shown in Figure 3(a), the initial dislocation density was extremely low, with most dislocations residing in the matrix and in the γ/γ' interfaces. The average dislocation density was measured to be $10^8/\text{cm}^2$ in the as-heat treated material, and very few of these dislocations were within the γ' precipitates.

Mechanical Behavior

Temperature Effects

As shown in Table 2 and Figure 4, the yield strength at 0.05% offset was the same at 20 and 705°C. Above 760°C, the strength began to drop rapidly, and the strain rate began to have a strong effect on the strength. The decrease in strength as a function of temperature was linear at 50%/min over the entire temperature range, and linear at 0.5%/min up to 927°C. Such behavior is typical of high volume fraction superalloys, and has been documented for several similar systems [8,10,19,59,60]. The results are also in reasonable agreement with those obtained for PWA 1480 in another study [12].

Strain Rate Effects

At 705°C and below, there was no effect of strain rate in the range tested (0.5 - 50%/min). At 760°C and above, strain rate became very important. At the lower strain rate, the strength began to fall at 760°C, while at the higher strain rate the strength did not begin to drop until above 815°C. At constant temperature, the strength was significantly lower for the slower strain rate. Similar trends have been reported in studies of the strain rate dependence of yielding in Mar-M 200 and Udimet 115 [19,59].

Data Correlation

As indicated by the strain rate and temperature dependence of the yield strength, yielding at elevated temperatures is a thermally activated process. It is therefore appealing to present the data in the form of an Arrhenius-type relationship. Rate-controlling mechanisms may then be deduced as a function of temperature. Figure 5 is a plot of the modulus-normalized yield strength vs inverse temperature, which represents an equation of the form $\ln(\sigma/E)$ vs $1/T$:

$$\sigma/E = A [\exp(Q'/RT)] , \quad (4-1)$$

where

σ = Yield strength,

Q' = Apparent activation energy,

A = A constant.

As illustrated by Figure 5, there are three distinct temperature regimes when the data are represented in this way:

- a) At low temperatures (below 760°C), Q' was equal to zero, so thermal activation was not a factor in the range of strain rates tested.
- b) At high temperatures (above 927°C at 50%/min and above 815°C at 0.5%/min) Q' was a constant equal to 50 kJ/mol, and was independent of strain rate. The true activation energy is calculated and discussed later in the paper.
- c) At intermediate temperatures, a transition from the low to the high temperature behavior occurred. It is evident from the shape of the curves that the transition region boundaries and functional forms were a strong function of strain rate.

Deformation Substructures

Analysis of the deformation substructures resulted in the same three temperature regimes as the Arrhenius analysis, and the boundaries of the three regimes were the same. As discussed below, low temperature deformation was

dominated by γ' shearing, high temperature deformation was dominated by γ' by-pass, and intermediate temperatures exhibited a transition from shearing to by-pass.

Low Temperatures

Deformation substructures at 20, 705, and 760°C (high strain rate only) were qualitatively similar. The dominant deformation mechanism was shearing of the γ' by pairs of $a/2\langle 110 \rangle$ dislocations which were confined to octahedral planes. At 20°C, relatively few dislocations were present at yield, and the spacing between dislocations was large, Figure 6(a). However, the dislocation density at yield was significantly higher than it was in the as-heat treated material. There was also evidence of γ' shearing, including the presence of dislocation pairs and residual loops within the γ' . At 705 and 760°C, the dislocation density at yield was very high, and the structure consisted of intense slip bands which contained closely spaced dislocations, Figure 6(b). It is possible that this type of structure may have been formed but not observed at 20°C, due to the possibility of extremely localized, non-homogeneous slip.

Through systematic analysis of the dislocation Burgers vectors and line directions, it was determined that the vast majority of dislocations observed after deformation at low temperatures were of the type $\{111\}a/2\langle 110 \rangle$. Dislocations travelled through the γ' as

closely-spaced pairs in order to minimize the anti-phase boundary (APB) area created by the $a/2\langle 110 \rangle$ displacement of the superlattice [15]. This is demonstrated by Figure 7, in which those portions of the dislocations within the precipitate are constricted due to the high APBE, while those portions of the same dislocations which had exited the precipitates are split due to the elastic repulsion. Figure 8 demonstrates that the γ' was sheared during deformation, as the precipitate exhibits a shear offset which is parallel to the projected the Burgers vector of the dislocations.

High Temperatures

The boundary for the high temperature region was a function of strain rate. At 0.5%/min, high temperature behavior was dominant at 815°C and above, while at 50%/min, high temperature behavior did not manifest itself until 927°C and above.

In contrast to the shearing which was observed at low temperatures, deformation at high temperatures occurred primarily by dislocations moving between and around the precipitates. Figure 9 shows a typical substructure consisting of dislocation loops left in the γ/γ' interface and in the γ matrix. The stereo pair in Figure 10 clearly shows groups of dislocations weaving between and wrapping around the γ' precipitates. Typical dislocation densities in this regime were measured to be 1×10^9 to $5 \times 10^9/\text{cm}^2$

after 0.3% plastic strain. Dislocations were very infrequently observed within the γ' after interrupted tests conducted at 0.5%/min above 815°C. Although a few slip bands were observed to have cut the γ' even at 1093°C, the dominant mechanism at low strain levels at 927°C and above was particle by-pass at both strain rates.

While dislocations were not observed within the γ' after interrupted tests at the low strain rate, the specimens which were tested to failure at 871 and 982°C contained a high density of dislocations within the γ' , Figure 11. This indicates that the first step in deformation was by-pass of the γ' , which was followed by shearing of the γ' later in the test. Shearing occurred only after large increases in the matrix dislocation density and significant strain hardening had occurred. This is discussed in more detail in the last section of this chapter.

The dislocations which became trapped in the γ/γ' interfaces were frequently observed to be pure edge dislocations lying on $\{011\}$ planes. This phenomenon was observed at every temperature, and was very common at 982 and 1093°C. An example is shown in Figure 12(a), where the majority of dislocations parallel to the cube edges were interfacial, with an $a/2[\bar{1}01]$ Burgers vector and a near-[010] line direction. This characterizes the dislocations as nearly pure edge, lying on the (101)

plane. By following the dislocations into the matrix, it was determined that they had cross-slipped from $\{111\}$ planes to $\{011\}$ planes at the interface. Pure edge dislocations lying on $\{011\}$ planes in the γ/γ' interfaces have been reported in a similar alloy after creep testing at 850°C , and it was proposed that thermally activated glide had occurred on $\{011\}$ planes in the matrix [61]. Our results suggest that such a mechanism did not occur in this study.

Pure edge dislocations create an elastic strain field with a dilatational component [62], so the total energy of the γ/γ' interface can be reduced if an edge dislocation of the appropriate sign lies in the interface and accommodates some of the lattice mismatch strain. It should also be noted that $\{011\}$ planes can easily accommodate pure edge dislocations with low index line directions, $\langle 100 \rangle$. This provides a driving force for cross-slip onto $\{011\}$ planes, which is not normally observed in FCC alloys.

At 1093°C , the interfacial dislocations coalesced to form a homogeneous, regular array after about 0.2% plastic strain, Figure 12(b). The networks were hexagonal in nature, and consisted of primarily two types of dislocations: Pure edge dislocations lying on $\{011\}$ planes with $\langle 100 \rangle$ line directions, and mixed dislocations lying on $\{111\}$ planes with $\langle 110 \rangle$ line directions. This network

was extremely stable. The specimen which was tested to failure (30% elongation) exhibited the same type of deformation substructure as the interrupted test specimen (0.2% plastic strain), Figure 13(a). The failed specimen contained finer networks and a few dislocations within the γ' , but the substructure was essentially the same as that of the interrupted test. In addition to a slight refinement of the interfacial networks, the γ' did coarsen slightly in localized regions.

The specimens tested under creep conditions at stresses equal to 70 - 80% of the low strain rate yield strength exhibited the same type of deformation substructures as those which developed during yielding. Figure 13(b) shows the substructure after creep testing at 1093°C and 117 MPa. The only difference between the tensile and creep deformation was the increased γ' coarsening during creep, Figure 13(b). The specimen which was creep tested at 871°C and 414 MPa developed the same type of interfacial arrays, but the γ' did not coarsen significantly.

It is evident not only that the deformation during creep and yielding was similar, but also that the steady-state deformation substructures developed at low plastic strain levels. The only difference between the substructures at 1093°C after 0.3% strain, after tensile failure, and after creep failure were slight refinements of

the interfacial networks, and coarsening of the γ' .

Intermediate Temperatures

Not surprisingly, a transition from shearing to bypass was observed in the range from 760 to 927°C (depending on strain rate). Slip bands were only observed at the high strain rate, and the slip band density decreased as the temperature increased.

Similar to observations in other alloys systems during creep at 760°C [21,22], γ' shearing by the $\{111\}\langle 112\rangle$ slip system was observed after slow strain rate testing at 760°C. Initially, the only operative deformation mechanism was slip of $a/2\langle 110\rangle$ dislocations in the matrix. At about 0.25% plastic strain, however, deformation also began to occur by slip of $\langle 112\rangle$ type partials through the γ' , resulting in the creation of stacking faults, Figure 14. The partial dislocations seen in Figure 14(a) were found to have a Burgers vector direction of $[1\bar{1}2]$, and the stacking faults were found to be intrinsic, lying on $(\bar{1}11)$. A superlattice-intrinsic stacking fault (S-ISF) can be formed in Ni_3Al by the glide of $\{111\}a/3\langle 112\rangle$ partials after the reaction

$$a/2[0\bar{1}1] = a/3[1\bar{1}2] + a/6[\bar{2}\bar{1}\bar{1}] \quad (4-2)$$

occurs [63]. Also, extrinsic/intrinsic "fault pairs" can be formed in some alloys by the glide of $a/3\langle 112\rangle$ partial

dislocations [21,22]. In this study, fault pairs were not found, and the faults were intrinsic in nature. It appears, therefore, that the dislocations creating the stacking faults were $(\bar{1}11)a/3[1\bar{1}2]$ partials, and Equation (4-2) represents the reaction which occurred in the γ/γ' interface.

Modeling of Yielding Process

It is evident from the preceding discussion that two distinct models of the yielding process in PWA 1480 must be applied: A low temperature model based on γ' shearing, and a high temperature model based on γ' by-pass. The intermediate temperature regime exhibited complex transitional behavior which was very dependent on strain rate, and would be difficult to model with the presently available experimental results.

Low Temperatures

At temperatures below 760°C, yielding was controlled by γ' shearing. However, the deformation microstructures at the yield point were not completely independent of temperature. At room temperature, the dislocation density was low, and there were relatively few dislocations within the γ' . At 705°C, the dislocation density was much higher, and there was a large number of dislocations within the γ' . This suggests that the rate-controlling step in the shearing process changed with temperature. As shown in

the following discussion, no currently available model of yielding can fully explain this behavior.

As discussed in Chapter II, few models are applicable in the shearing regime for alloys such as PWA 1480, due to the high volume fraction of γ' and the large particle size. The two models which may be applied are the Huther-Reppich model [45-47] and the Copley-Kear model [11]. Both models neglect the contribution of misfit strengthening. In PWA 1480 such an assumption is fairly reasonable, due to the relatively low lattice parameter mismatch of 0.28% (extracted γ') [64]. When applied to PWA 1480, both models predict a similar form for the critical resolved shear stress (CRSS).

The major reason that most precipitation hardening models are not applicable at high volume fractions is that they are based on solid solution strengthening models which were developed for dilute arrays of point obstacles. Huther and Reppich [45-47] have developed a model which attempts to overcome this. They derived their model from the solid solution strengthening model of Schwarz and Labusch [48], which treats both dilute arrays and concentrated arrays of obstacles. An additional strong point of the Huther-Reppich model is that it allows for a transition from "weak" dislocation pair coupling to "strong" dislocation pair coupling above a critical particle size. "Strong" pair coupling, which implies that

both the leading and trailing dislocations are in the same particle during shearing, occurs in PWA 1480 (Figure 7). The equation for the increase in the CRSS due to precipitates when "strong" pair coupling occurs is given by Equation (2-7):

$$\Delta\tau_c = 0.86 \{ (Tf^{1/2}w)/bd \} \{ (1.28 d\gamma_o/wT) - 1 \}^{1/2} . \quad (4-3)$$

At very large particle sizes, the stress necessary to cause the first dislocation to penetrate the particle can become larger than the CRSS predicted by Equation (4-3), and can therefore dominate the CRSS. The penetration stress is given by Equation (2-8):

$$\Delta\tau_c = (\gamma_o/b) - (T/br_s) . \quad (4-4)$$

By using the constant line tension approximation,

$$T = Gb^2/2 , \quad (4-5)$$

where G = Shear modulus, Equation (4-4) becomes

$$\Delta\tau_c = (\gamma_o/b) - (Gb/2r_s) . \quad (4-6)$$

By substituting reasonable values for PWA 1480, it is found that the penetration stress, Equation (4-6), is much larger

that the shearing stress, Equation (4-3). (See Appendix C). Therefore, the precipitates cannot be treated as weak obstacles, and Equation (4-6) should predict the CRSS according to this theory.

Copley and Kear's penetration stress is given by Equation (2-9):

$$\tau_C = (\gamma_O/2b) - (T/br_s) + 1/2(\tau_m + \tau_p) . \quad (4-7)$$

Since $1/2 (\tau_m + \tau_p)$ may be considered an average Peierls stress when V_f is about 0.5, Equation (4-7) may be written as follows (after substituting the constant line tension approximation):

$$\Delta\tau_C = (\gamma_O/2b) - (Gb/2r_s) . \quad (4-8)$$

The only difference between Equations (4-6) and (4-8) is the factor of 1/2 in the APB term, which arises from the fact that Copley and Kear considered both the leading and trailing dislocations in their force balance, and it appears that Huther and Reppich only considered the leading dislocation in their analysis. As shown in Appendix C, the Copley-Kear penetration stress predicts the CRSS for PWA 1480 more accurately than the Huther-Reppich penetration stress.

Equation (4-7) has been used to model the

temperature dependence of the CRSS in Mar-M 200 [10,11].

It was postulated that the CRSS was independent of temperature up to 760°C because:

- i) γ_0 was independent of temperature,
- ii) $Gb/2r_s$ changed negligibly from 20-760°C,
- iii) $\Delta(\tau_m + \tau_p) = 0$ from 20-760°C,
- iv) The rate controlling mechanism was penetration at all temperatures.

The major problem with using this approach to model the temperature dependence of the yield strength of PWA 1480 is the assumption that penetration into the particle is rate controlling at all temperatures. Figures 6-8 show that at intermediate temperatures, about 8-10 dislocations were able to penetrate the γ' particle before the first dislocation was able to completely shear it. This implies that the CRSS of the particle was more important than the penetration stress, and therefore a new type of temperature-dependent model must be developed. This is a goal for future research.

High Temperatures

At high temperatures, plastic flow occurred during yielding by γ' by-pass. Under these conditions, the rate-limiting step in many systems is diffusion-controlled climb [27,29,30,37,50,65]. The true activation energy for yielding at high temperature in PWA 1480, which is

calculated to be 500 kJ/mol in Appendix D, indicates that self-diffusion was probably the rate limiting step in the yielding process (See discussion in Appendix D). Thus, both the activation energy analysis and the microstructural evidence for by-pass provide a strong argument for dislocation climb as the rate-limiting step during yielding, and a model of yielding based on γ' by-pass which is controlled by climb is appropriate.

As discussed in Chapter II, Brown and Ham [37] have proposed such a model for a system of cuboidal precipitates. Although the model does not quantitatively predict the actual CRSS except for low volume fraction alloys, its functional form with respect to temperature does agree with the results of the present study. The CRSS is given by Equation (2-9), and its functional form with respect to temperature is:

$$\tau_c = \tau_0 + k_1 Q_D - k_2 T |\ln(k_3 \dot{\epsilon})| , \quad (4-9)$$

where

- τ_0 = Threshold stress which depends on the type of microstructure,
- Q_D = Activation energy of the rate controlling diffusion process,
- k_i = Constants which include microstructural parameters.

Equation (4-9) predicts a linear decrease in CRSS with temperature, which is observed except above 982°C at the slow strain rate (Figure 4). However, it must be noted that Equation (4-9) is not applicable at the high strain rate until above 927°C, even though the linear relationship starts as low as 815°C. This is clear because the transition region at the higher strain rate did not end until 927°C, and γ' shearing was important in the transition regime.

It is not clear why the yield strength vs temperature relationship deviates from linearity above 982°C at the slow strain rate. One possibility is that the threshold stress is being approached, and the curve is reaching an asymptotic limit. Brown and Ham argue that there is always a finite yield stress, which is due to the force necessary to create additional dislocation line length during the climb process. Another possible reason for the deviation from linearity is related to the deformation mechanisms: The temperature where the deviation from linearity begins to occur is the same temperature at which the {011} interfacial dislocations became common and the interfacial networks began to develop. It is feasible that the attractive force between the interface and the climbing dislocation could reduce the climb rate, thus increasing the CRSS. The Brown-Ham model was derived for mismatch-free precipitates, and this type

of interaction is not considered in their model.

Micro-Mechanics of Yielding

The plastic strain introduced into a crystal can be calculated by [76]:

$$\gamma = b\rho\lambda , \quad (4-10)$$

where γ = Plastic shear strain,
 ρ = Mobile dislocation density,
 λ = Dislocation mean free path.

In the as-received material, the dislocation density was measured to be $10^8/\text{cm}^2$, while $b = 2.5 \times 10^{-8}$ cm. The mean free path, λ , may be calculated by the following equation [58]:

$$\lambda = (1 - V_f)/N_L , \quad (4-11)$$

where N_L is the number of particles per unit length. In PWA 1480, N_L was calculated to be $1.64/\mu\text{m}$, so the mean free path of each dislocation is calculated to be $0.25 \mu\text{m}$.

Assuming that all the dislocations initially in the material are mobile, the shear strain that is possible in the material without γ' shearing, dislocation climb, or

increases in ρ can be calculated:

$$\gamma = b\rho\lambda = 0.006\% . \quad (4-12)$$

Obviously, the initial dislocation density is not sufficient to cause measurable macroscopic yielding in the absence of shearing or thermal activation. Both of these factors influence the yield strength of PWA 1480, depending on the temperature.

At low temperatures (below 760°C), dislocation climb and particle by-pass are not dominant mechanisms, so the γ' particles must be sheared to obtain measurable plastic strain. This is seen clearly in Figures 6-8. Additionally, it is seen that there was a significant increase in the dislocation density even at plastic strain levels as low as 0.1% at 705°C.

At high temperatures, dislocation climb aided the by-pass process during yielding. The result of this was an effective increase in λ , which increased the amount of plastic strain that could occur before shearing took place. Also, fewer dislocations were necessary to carry the yield strain, which correlates very well with the observed lower dislocation densities at higher temperatures.

CHAPTER V

SUMMARY AND CONCLUSIONS

Mechanical Behavior

The yield strength trends of PWA 1480 as a function of temperature and strain rate were similar to other high volume fraction superalloys. The strength was constant and independent of strain rate up to 760°C, above which the strength dropped rapidly and became a strong function of strain rate.

The yield strength vs temperature was correlated very well by an Arrhenius-type relationship. This resulted in three temperature regimes, and the boundaries were a function of strain rate. At low temperatures, the yield strength was independent of temperature. At high temperatures, the slope of the Arrhenius curve was independent of strain rate, and the activation energy for yielding was indicative of a self-diffusion controlled process. At intermediate temperatures, the shape of the Arrhenius curve was a function of strain rate, and represented a transition from low to high temperature behavior.

Dominant Deformation Mechanisms

The deformation substructures at yield can be divided into the same three temperature regimes. At low temperatures, deformation occurred by shearing of the γ' by pairs of $a/2\langle 110 \rangle$ dislocations on $\{111\}$ planes. At high temperatures, deformation was dominated by particle by-pass by single $a/2\langle 110 \rangle$ dislocations. At intermediate temperatures, a transition from shearing to by-pass occurred. Since classification of the deformation substructures resulted in the same three temperature regimes as the Arrhenius analysis, it is clear that there was a fundamental relationship between deformation mechanisms and activation energies. The dominant deformation mechanisms could be related fundamentally to the observed microstructural parameters and dislocation densities.

Detailed Substructures

As the temperature was increased from 20 to 760°C, the dislocation density at yield increased, and many dislocations were within the γ' when the test was interrupted at 705 and 760°C. At 760°C and a strain rate of 0.5%/min, intrinsic stacking faults were produced in the γ' by shearing by $a/3\langle 112 \rangle$ partial dislocations. At temperatures above about 870°C, many dislocations cross-

slipped from $\{111\}$ to $\{011\}$ planes in the γ/γ' interface. Most $\{011\}$ plane dislocations were found to be nearly pure edge in character, which allows the dislocations to accomodate the lattice mismatch strain and thereby reduce the interfacial energy. At 982 and 1093°C, this leads to the formation of stable hexagonal networks in the interface. These interfacial networks were also developed during creep at 871 and 1093°C. In this temperature regime, there was very little difference between the deformation substructures at yield, after tensile failure, and after creep failure. At 815 to 982°C, however, the substructures developed during tensile testing were a strong function of strain level: By-pass was observed at yield, while shearing was evident later in the test. γ' coarsening occurred during slow strain rate tensile testing at 1093°C and creep testing at 871 and 1093°C.

Modeling of Yielding

To model the yielding behavior, the same three temperature regimes must be considered. At low temperatures, a model based on γ' shearing is needed, and two applicable models are available. When applied to PWA 1480, both models predict the CRSS based on the premise that penetration into the particle is the rate-limiting step. However, our results show that penetration was not the rate-limiting step in PWA 1480 at 705 and 760°C, so a

new model must be developed. At high temperatures, a model based on γ' by-pass is needed. The deformation substructures and calculated activation energies imply that the theory of Brown and Ham was valid, and the functional form of the model fit the data well. However, their model must be modified at very high temperatures in order to be fully applicable to PWA 1480. The intermediate temperature regime exhibited complex transitional behavior which was very dependent on strain rate, and would be difficult to model with the presently available data.

slipped from {111} to {011} planes in the γ/γ' interface. Most {011} plane dislocations were found to be nearly pure edge in character, which allows the dislocations to accommodate the lattice mismatch strain and thereby reduce the interfacial energy. At 982 and 1093°C, this leads to the formation of stable hexagonal networks in the interface. These interfacial networks were also developed during creep at 871 and 1093°C. In this temperature regime, there was very little difference between the deformation substructures at yield, after tensile failure, and after creep failure. At 815 to 982°C, however, the substructures developed during tensile testing were a strong function of strain level: By-pass was observed at yield, while shearing was evident later in the test. γ' coarsening occurred during slow strain rate tensile testing at 1093°C and creep testing at 871 and 1093°C.

Modeling of Yielding

To model the yielding behavior, the same three temperature regimes must be considered. At low temperatures, a model based on γ' shearing is needed, and two applicable models are available. When applied to PWA 1480, both models predict the CRSS based on the premise that penetration into the particle is the rate-limiting step. However, our results show that penetration was not the rate-limiting step in PWA 1480 at 705 and 760°C, so a

new model must be developed. At high temperatures, a model based on γ' by-pass is needed. The deformation substructures and calculated activation energies imply that the theory of Brown and Ham was valid, and the functional form of the model fit the data well. However, their model must be modified at very high temperatures in order to be fully applicable to PWA 1480. The intermediate temperature regime exhibited complex transitional behavior which was very dependent on strain rate, and would be difficult to model with the presently available data.

REFERENCES

1. R.W. Fawley: "Superalloy Progress", in The Superalloys, C.T. Sims and W.C. Hagel, eds., Wiley, New York, 1972, pp. 3-29.
2. M. Gell, D.N. Duhl, and A.F. Giamei: "The Development of Single Crystal Superalloy Turbine Blades", in Superalloys 1980, Proc. 4th Intl. Symposium on Superalloys, J.K. Tien et.al., eds., ASM, Metals Park, Ohio, pp. 205-214.
3. "Single Crystal Blades Produce Gains in Durability", Aviation Week and Space Technology, June 28, 1982, p. 205-207.
4. W.T. Chandler: "Materials for Advanced Rocket Engine Turbopump Turbine Blades", NASA CR-174729, 1983.
5. R.F. Decker and C.T. Sims: "The Metallurgy of Nickel-Base Alloys", in The Superalloys, C.T. Sims and W.C. Hagel, eds., Wiley, New York, 1972, pp. 33-77.
6. R.F. Decker: Strengthening Mechanisms in Nickel-Base Superalloys, International Nickel Co., New York, 1970.
7. B.J. Piarcey, B.H. Kear, and R.W. Smashey: "Correlation of Structure with Properties in a Directionally Solidified Nickel-Base Superalloy", Trans. ASM, 1967, vol. 60, pp. 634-645.
8. P. Beardmore, R.G. Davies, and T.L. Johnston: "On the Temperature Dependence of the Flow Stress of Nickel-Base Alloys", Trans. TMS-AIME, 1969, vol. 245, pp. 1537-1545.
9. B.H. Kear and B.J. Piarcey: "Tensile and Creep Properties of Single Crystals of the Nickel-Base Superalloy Mar-M 200", Trans. TMS-AIME, 1967, vol. 239, pp. 1209-1215.
10. S.M. Copley, B.H. Kear, and G.M. Rowe: "The Temperature and Orientation Dependence of Yielding in Mar-M 200 Single Crystals", Mater. Sci. Eng., 1972, vol. 10, pp. 87-91.

11. S.M. Copley and B.H. Kear: "A Dynamic Theory of Precipitation Hardening with Application to Nickel-Base Superalloys", Trans. TMS-AIME, 1967, vol. 239, pp. 984-992.
12. D.M. Shah and D.N. Duhl: "The Effect of Orientation, Temperature, and γ' Size on the Yield Strength of a Single Crystal Nickel-Base Superalloy", in Superalloys 1984, Proc. 5th Intl. Symposium on Superalloys, M. Gell et.al., eds., AIME, Warrendale Pa., 1984, pp. 105-114.
13. S.M. Copley and B.H. Kear: "Temperature and Orientation Dependence of the Flow Stress in Off-Stoichiometric Ni_3Al ", Trans. TMS-AIME, 1967, vol. 239, pp. 977-984.
14. C. Lall, S. Chin, and D.P. Pope: "The Orientation and Temperature Dependence of the Yield Stress of $\text{Ni}_3(\text{Al}, \text{Nb})$ Single Crystals", Metall. Trans. A, 1979, vol. 10A, pp. 1323-1332.
15. P.A. Flinn: "Theory of Deformation in Superlattices", Trans TMS-AIME, 1960, vol. 218, pp. 145-154.
16. S. Takeuchi and E. Kuramoto: "Temperature and Orientation Dependence of the Yield Stress of Ni_3Ge Single Crystals", Acta Metall., 1973, vol. 21, pp. 415-425.
17. D.A. Grose and G.S. Ansell: "The Influence of Coherency Strains on the Elevated Temperature Tensile Behavior of Ni-15Cr-Al-Ti-Mo Alloys", Metall. Trans. A, 1981, vol. 12A, pp. 1631-1645.
18. N.S. Stoloff: "Fundamentals of Strengthening", in The Superalloys, C.T. Sims and W.C. Hagel, eds., Wiley, New York, 1972, pp. 79-111.
19. G.R. Leverant, M. Gell, and S.W. Hopkins: "The Effect of Strain Rate on the Flow Stress and Dislocation Behavior of a Precipitation Hardened Nickel-Base Superalloy", Mater. Sci Eng., 1971, vol. 8, pp. 125-133.
20. R.R. Jensen, T.E. Howson, and J.K. Tien: "Very Slow Strain Rate Stress-Strain Behavior and Resisting Stress for Creep in a Nickel-Base Superalloy", in Superalloys 1980, Proc. 4th Intl. Symposium on Superalloys, J.K. Tien et.al., eds, ASM, Metals Park, Ohio, 1980, pp. 679-688.

21. B.H. Kear, J.M. Oblak, and A.F. Giamei: "Stacking Faults in γ' ($\text{Ni}_3(\text{Al}, \text{Ti})$) Precipitation Hardened Nickel-Base Superalloy", Metall. Trans., 1970, vol. 1, pp. 2477-2486.
22. G.R. Leverant and B.H. Kear: "The Mechanism of Creep in a γ' Precipitation Hardened Nickel-Base Superalloy at Intermediate Temperatures", Metall. Trans., 1970, vol. 1, pp. 491-498.
23. G.R. Leverant, B.H. Kear, and J.M. Oblak: "The Influence of Matrix Stacking Fault Energy on Creep Deformation Modes in γ' Precipitation Hardened Nickel-Base Superalloys", Metall. Trans., 1971, vol. 2, pp. 2305-2306.
24. G.R. Leverant and D.N. Duhl: "The Effect of Stress and Temperature on the Extent of Primary Creep in Directionally Solidified Nickel-Base Superalloys", Metall. Trans., 1971, vol. 2, pp. 907-908.
25. R.A. MacKay and R.D. Maier: "The Influence of Orientation on the Stress Rupture Properties of Nickel-Base Superalloy Single Crystals", Metall. Trans. A, 1982, vol. 13A, pp. 1747-1754.
26. G.R. Leverant, B.H. Kear, and J.M. Oblak: "Creep of Precipitation Hardened Nickel-Base Superalloy Single Crystals at High Temperatures", Metall. Trans., 1973, vol. 4, pp. 355-362.
27. C. Carry and J.L. Strudel: "Apparent and Effective Creep Parameters in Single Crystals of a Nickel-Base Superalloy II: Secondary Creep", Acta Metall., 1978, vol. 26, pp. 859-870.
28. G. Jiantiang et. al.: "An Investigation in the Creep and Fracture Behavior of the Cast Nickel-Base Superalloy In738LC", Metall. Trans. A, 1983, vol. 14A, pp. 2329-2335.
29. R.A. Stevens and P.E.J. Flewitt: "The Dependence of the Creep Rate on Microstructure in a γ' Strengthened Superalloy", Acta Metall., 1981, vol. 29, pp. 867-882.
30. P.J. Henderson and M. McClean: "Microstructural Contributions to Friction Stress and Recovery Kinetics During Creep of the Nickel-Base Superalloy In738LC", Acta Metall., 1983, vol. 31, pp. 1203-1219.

31. P. Beardmore, R.G. Davies, and T.L. Johnston: "On the Temperature Dependence of the Flow Stress in Nickel-Base Alloys", Trans.TMS-AIME, 1969, vol. 245, pp. 1537-1545.
32. J.K. Tien and S.M. Copley: "The Effect of Uniaxial Stress On the Periodic Morphology of Coherent γ' Precipitates in Nickel-Base Superalloy Single Crystals", Metall. Trans., 1971, vol. 2, pp. 215-219.
33. D.D. Pearson, F.D. Lemkey, and B.H. Kear: "Stress Coarsening of γ' and its Influence on Creep Properties of a Single Crystal Superalloy", in Superalloys 1980, Proc. 4th Intl. Symposium on Superalloys, J.K. Tien et.al., eds., ASM, Metals Park, Ohio, 1980, pp. 513-520.
34. R.A. MacKay and L.J. Ebert: "The Development of Directional Coarsening of the γ' Precipitate in Superalloy Single Crystals", Scripta Metall., 1983, vol. 17, pp. 1217-1222.
35. P. Caron and T. Khan: "Improvement of Creep Strength in a Nickel-Base Superalloy by Heat Treatment", Mater. Sci. Eng., 1983, vol. 61, pp. 173-184.
36. H. Gleiter and E. Hornbogen: Physica Stat. Sol., 1965, vol. 12, p. 235.
37. L.M. Brown and R.K. Ham: "Dislocation-Particle Interactions", in Strengthening Methods in Crystals, A. Kelly and R.B. Nicholson, eds., Wiley, New York, 1971, pp. 9-134.
38. D. Raynor and J.M. Silcock: "Strengthening Mechanisms in γ' Precipitating Alloys", Metal Sci. J., 1970, vol. 4, pp. 121-130.
39. A. Melander and P.A. Persson: "Strength of a γ' Hardened Nickel-Base Alloy", Metal Sci., 1978, vol. 12, pp. 391-398.
40. V. Munjall and A.J. Ardell: "Precipitation Hardening of Ni-12.9% Al Alloy Single Crystals", Acta Metall., 1975, vol. 23, pp. 543-520.
41. V.A. Phillips: "Hardening Mechanisms in a Precipitation Hardening Nickel-12.7% Aluminum Alloy", Phil. Mag., 1967, vol. 16, pp. 103-117.

42. A.J. Ardell, V. Munjall, and D.J. Chellman:
"Precipitation Hardening of Ni-Al Alloys Containing
Large Volume Fractions of γ' ", Metall. Trans. A,
1976, vol. 7A, pp. 1263-1268.
43. R.L. Fleischer: "Substitutional Solution Hardening",
Acta Metall., 1963, vol. 11, pp. 203-210.
44. R.B. Schwarz and R. Labusch: "Dynamic Simulation of
Solution Hardening", J. Appl. Physics, 1978,
vol. 49, pp. 5174-5187.
45. B. Reppich: "Some New Aspects Concerning Particle
Hardening Mechanisms in γ' Precipitating Nickel-
Base Alloys - I. Theoretical Concepts", Acta Metal.,
1982, vol. 30, pp. 87-94.
46. W. Huther and B. Reppich: "Order Hardening of MgO by
Large Volume Fractions of Spinel Particles", Mater.
Sci. Eng., 1979, vol. 39, pp. 247-259.
47. W. Huther and B. Reppich: Z. Metallk., 1978, vol. 69,
p. 628.
48. B. Reppich, P. Schepp, and G. Wehner: "Some New Aspects
Concerning Particle Hardening Mechanisms in γ'
Precipitating Nickel-Base Alloys - II. Experiments",
Acta Metall., 1982, vol. 30, pp. 95-104.
49. P. Haasen and R. Labusch: "Precipitation Hardening by
Large Volume Fractions of Ordered Particles", in
Strength of Metals and Alloys, Proc. 5th Intl.
Conference on the Strength of Metals and Alloys,
Aachen, FRG, 1979, vol. 1, pp. 639-643.
50. G. Ansell and J. Weertman: "Creep of a Dispersion-
Hardened Aluminum Alloy", Trans. TMS-AIME, 1959,
vol. 215, pp. 838-843.
51. R.S.W. Shewfelt and L.M. Brown: "High Temperature
Strength of Dispersion-Hardened Single Crystals - II.
Theory", Phil. Mag., 1977, vol. 35, pp. 945-962.
52. V.A. Phillips: "Hardening Mechanisms in a Precipitation
Hardening Nickel-12.7% Aluminum Alloy", Phil. Mag.,
1967, vol. 16, pp. 103-117.
53. R.F. Miller and G.S. Ansell: "Low Temperature
Mechanical Behavior of Ni-15Cr-Al-Ti-Mo Alloys",
Metall. Trans. A, 1977, vol. 8A, pp. 1979-1991.

54. D.A. Grose and G.S. Ansell: "The Influence of Coherency Strains on the Elevated Temperature Tensile Behavior of Ni-15Cr-Al-Ti-Mo Alloys", Metall. Trans. A, 1981, vol. 12A, pp. 1631-1645.
55. R.F. Decker and J.R. Mihalisin: "Coherency Strains in γ' Hardened Nickel Alloys", Trans. ASM, 1969, vol. 62, pp. 481-489.
56. G.N. Maniar and J.E. Bridge: "Effect of γ/γ' Mismatch Volume Fraction γ' , and γ' Morphology on Elevated Temperature Properties of Ni-20Cr-5.5Mo-Ti-Al Alloys", Metall. Trans., 1971, vol. 2, pp. 95-102.
57. G.N. Maniar et.al.: "Correlation of γ/γ' Mismatch and Strengthening in Ni/Fe-Ni Base Alloys Containing Aluminum and Titanium as Hardeners", Metall. Trans., 1970, vol. 1, pp. 31-42.
58. E.E. Underwood: Quantitative Stereology, Addison-Wesley, Reading, Mass., 1970, pp. 23-44.
59. R.R. Jensen, T.E. Howson, and J.K. Tien: "Very Slow Strain Rate Stress-Strain Behavior and Resisting Stress for Creep in a Nickel-Base Superalloy", in Superalloys 1980, Proc. 4th Intl. Symposium on Superalloys, J.K. Tien et.al., eds., ASM, Metals Park, Ohio, 1980, pp. 679-688.
60. M.V. Nathal, R.D. Maier, and L.J. Ebert: "The Influence of Cobalt on the Tensile and Stress-Rupture Properties of the Nickel-Base Superalloy Mar-M 247", Metall. Trans. A, 1982, vol. 13A, pp. 1767-1774.
61. C. Carry and J.L. Strudel: "Direct Observation of $\langle 110 \rangle \{110\}$ Slip in FCC Single Crystals of a Nickel-Base Superalloy", Scripta Metall., 1975, vol. 9, pp. 731-736.
62. J. Weertman and J.R. Weertman: Elementary Dislocation Theory, MacMillan, New York, 1964, pp. 32-35.
63. P. Veysierre, J. Douin, and P. Beauchamp: "On the Presence of Superlattice-Intrinsic Stacking Faults in Plastically Deformed Ni_3Al ", Phil. Mag. A, 1985, vol. 51, pp. 469-483.
64. R.R. Bowman: M.S. Thesis, Georgia Institute of Technology, Atlanta, Ga., 1986, p. 135.

65. J.H. Hausselt and W.D. Nix: "A Model for High Temperature Deformation of Dispersion Strengthened Metals Based on Substructural Observations in Ni-20Cr-2ThO₂", Acta Metall., 1977, vol. 25, pp. 1491-1502.
66. P. Hirsch et.al.: Electron Microscopy of Thin Crystals, 2nd Ed., Krieger, Malabar, Fla., 1977.
67. J.W. Edington: Practical Electron Microscopy in Materials Science, VanNostrand Reinhold, New York, 1976.
68. A.F. Giamei: "Deformation and Fracture of Advanced Anisotropic Superalloys", AFOSR FR-12637, 1979.
69. D.N. Duhal: Private Communication, Pratt & Whitney Aircraft, E. Hartford, Conn., 1985.
70. G.A. Webster and B.J. Pearcey: "An Interpretation of the Effects of Stress and Temperature on the Creep Properties of a Nickel-Base Superalloy", Metal Sci. J., 1967, vol. 1, pp. 97-104.
71. A.K. Mukherjee, J.E. Bird, and J.E. Dorn: "Experimental Correlations for High Temperature Creep", Trans. ASM, 1969, vol. 62, pp. 155-179.
72. G.A. Swanson et.al.: HOST Annual Report, NASA CR-174952, 1985.
73. S. Purushothaman and J.K. Tien: "Role of Back Stress in the Creep Behavior of Particle Strengthened Alloys", Acta Metall., 1978, vol. 26, pp. 519-528.
74. T.E. Howson, D.A. Mervyn, and J.K. Tien: "Creep and Stress-Rupture of Mechanically Alloyed Oxide Dispersion and Precipitation Strengthened Nickel-Base Superalloys", Metall.Trans. A, 1980, vol. 11A, pp. 1609-1616.
75. M.V. Nathal and L.J. Ebert: "Elevated Temperature Creep Rupture of the Single Crystal Superalloy NASAIR 100", Metall. Trans. A, 1985, vol. 16A, pp. 427-440.
76. W.G. Johnston and J.J. Gilman: "Dislocation Velocities, Dislocation Densities, and Plastic Flow in LiF Crystals", J. Appl. Physics, 1959, vol. 30, pp. 129-144.

APPENDIX A
DETERMINATION OF CRYSTAL
ORIENTATION IN THE TEM

The crystallographic orientation of the grain within a thin foil can be determined in-situ in the TEM, thus facilitating diffraction experiments and dislocation analysis. The steps necessary to determine the orientation are briefly outlined below, then discussed in detail individually.

1. Determine the holder tilt axis on the TEM screen.
2. Tilt the crystal until a strongly diffracting, low index spot appears. Center the Kikuchi band directly over the transmitted spot.
3. Determine the Miller indices of the spot.
4. Measure the angle between the g-vector and the tilt axis. Record this angle, as well as the amount of tilt and sense of the tilt.
5. Plot the g-vector on a Wulff net.
6. Repeat Steps 2-5 two to three times.
7. Construct the stereographic projection
from the poles plotted in Step 5.

Each step will now be discussed in detail.

Step 1

The tilt axis was determined prior to this research, and is inscribed in the TEM viewing screen. This was done by measuring the trajectory of the Kikuchi lines during tilting of a crystal, and noting that the tilt axis is perpendicular to this trajectory. Figure 15 shows the screen schematically. Two quadrants are named (NW and SW) to facilitate angular record keeping.

Step 2

It is essential that the Kikuchi band be centered on the transmitted spot, thus ensuring that the diffracting planes are parallel to the electron beam.

Step 3

The d-spacing of the diffracting planes can be determined from the spacing "R" between the transmitted and diffracted beams by the following equation [66,67]:

$$\lambda L = R d , \quad (A-1)$$

where λ = Electron wavelength,
 L = Camera length,
 R = Spot spacing,
 d = d-spacing.

The g-vector can be determined from the d-spacing by the

following equation (for cubic crystals):

$$1/d^2 = (h^2 + k^2 + l^2)/a^2, \quad (A-2)$$

where a = Lattice parameter,

$[hkl]$ = Miller indices.

The viewing screen had two semicircles inscribed whose radii corresponded to the R for $\langle 111 \rangle$ and $\langle 220 \rangle$ g-vectors in nickel, which allowed visual determination of the g-vector.

Step 4

The angle between the tilt axis and the g-vector is recorded, and the quadrant in which the g-vector lies is recorded.

Step 5

The Wulff net is set up as follows (Figure 15(b)): The tilt axis is the North/South great circle; the beam direction is the center of the Wulff net; a clockwise rotation of the tilting stage tilts the crystal from West to East on the Wulff net. Thus, if diffraction occurs when the holder is tilted clockwise, the pole was in the Eastern half of the Wulff net at zero tilt, and if diffraction occurs when the holder is tilted counter-clockwise, the pole was in the Western half of the Wulff net at zero tilt.

The poles are plotted in the following way. Assume that diffraction occurs in the Northwest quadrant after a clockwise tilt of θ degrees, and the angle between the tilt axis and the g-vector was measured to be ϕ degrees. Starting at the North pole, travel clockwise along the outer great circle (the perimeter of the Wulff net) for ϕ degrees. Now, travel inward along the small circle for θ degrees. The pole is plotted at that point. Figure 15 illustrates the details of this procedure, and an example is given later in this appendix.

Steps 6 + 7

At least three low-index poles must be plotted, after which the stereographic projection is plotted in the normal way. The finished projection represents the orientation of the crystal when looking down along the electron beam at zero degrees tilt and rotation.

Example

A $\langle 001 \rangle$ zone axis appeared when the crystal was tilted 10° counter-clockwise (One is not normally so fortunate). The following data were measured (Figure 16(a)):

g	θ	ϕ	Quadrant
<200>	10°CCW	25°	SW
<220>	10°CCW	20°	NW
<200>	10°CCW	65°	NW

The first <200> pole is plotted by travelling 25° CCW from the North pole, then travelling 10° inward, Figure 16(b). The other two poles are plotted in a similar manner, and the projection is constructed, Figure 16(c).

APPENDIX B

DISLOCATION AND STACKING FAULT ANALYSIS

Dislocations Burgers vectors, line directions, and slip planes may be determined by a series of diffraction experiments in the TEM. In a similar fashion, the character and displacement vectors of stacking faults, as well as their habit planes, may be determined. This appendix reviews these procedures. Several textbooks offer more thorough treatments [66,67].

Determination of g-vector

Due to the electromagnetic nature of the lenses, the brightfield image is rotated with respect to the diffraction pattern, and the rotation is a function of magnification. The rotation is calibrated, so crystal directions which are observed in diffraction mode may be transferred to brightfield micrographs. An example is given in Figure 17. The original magnification was 66,000X, and the camera length in diffraction mode was 76 cm. From the pre-determined rotation calibration, the diffraction pattern was rotated 48° CW with respect to the micrograph. The g-vector direction seen in the diffraction pattern was then rotated 48° CCW and placed on the

micrograph.

Determination of Displacement Vectors

Under two-beam conditions, dislocation contrast will result unless the displacement field of the defect lies solely within the diffracting plane. This occurs when the " $\underline{g} \cdot \underline{b} = 0$ invisibility criterion" is satisfied:

$$\underline{g} \cdot (\underline{b} \times \underline{u}) = 0 , \quad (B-1)$$

where \underline{g} = Diffraction vector,
 \underline{u} = Line direction of dislocation.

Only residual contrast will result if

$$\underline{g} \cdot \underline{b} = 0 . \quad (B-2)$$

Therefore, the Burgers vector of a dislocation can be determined when two two-beam conditions are found which satisfy Equations (B-1) or (B-2). The Burgers vector will be the cross-product of the two \underline{g} -vectors.

Similarly, the displacement vector of a stacking fault can be determined by finding two two-beam conditions where the following criterion is satisfied:

$$\underline{g} \cdot \underline{R}_f = 0 , \quad (B-3)$$

where \underline{R}_f is the fault displacement vector. Additionally, a stacking fault can be nearly invisible when it is viewed edge-on.

For example, consider the dislocations labelled A, B, and C in Figure 18. Dislocation A disappears when $\underline{g} = [\bar{1}11]$ and $[220]$, so

$$\underline{b}_A = [\bar{1}11] \times [220] = [\bar{1}1\bar{2}] . \quad (B-4)$$

As discussed in the Chapter III, the actual Burgers vector was $a/3[\bar{1}1\bar{2}]$. Similarly,

$$\underline{b}_B = [200] \times [\bar{1}11] = a/2[0\bar{1}1] , \quad (B-5)$$

$$\text{and} \quad \underline{b}_C = [020] \times [\bar{1}11] = a/2[101] . \quad (B-6)$$

The stacking fault seen in Figure 18 was found to have $\underline{R}_f = [\bar{1}11]$, because the fault was found to be edge-on when $\underline{g} = [\bar{1}11]$. This was determined by tilting the crystal and measuring angles between the fault and the \underline{g} -vectors. The measured fault vector is also consistent with the invisibility when $\underline{g} = [220]$, because $[\bar{1}11] \cdot [220] = 0$.

Determination of Line Directions

The true line direction, \underline{u} , always lies in the plane defined by the beam direction, \underline{B} , and the projected line direction, \underline{u}_p . Therefore, a dislocation line direction can be determined by finding two or more conditions where \underline{u}_p and \underline{B} are known:

$$\underline{u} = (\underline{u}_p^1 \times \underline{B}_1) \times (\underline{u}_p^2 \times \underline{B}_2) . \quad (B-7)$$

This procedure is easier to conduct by using the stereographic projection than by using Equation (B-7). The procedure is as follows:

1. Determine the crystal orientation.
2. Tilt the crystal until a two-beam condition occurs where the dislocation shows contrast. Record the tilt settings in order to determine the beam direction.
3. Measure the angle between the g-vector and \underline{u}_p .
4. On a standard $\langle 001 \rangle$ projection, plot \underline{B} and \underline{u}_p . Draw a great circle between the two.
5. Repeat Steps (2-4) for at least 2 more g-vectors.
6. The intersection of the great circles determines \underline{u} .

For example, consider Dislocation C in Figure 18. The three g -vectors used were $[200]$, $[\bar{2}20]$, and $[111]$, but the $[111]$ micrograph is not shown in Figure 18. The crystal orientation was determined, and is shown in Figure 19. The following data were recorded from the two-axis tilting stage:

g	Tilt 1	Tilt 2	
$[200]$	24° W+E	9° S+N	
$[\bar{2}20]$	18° W+E	0	(B-8)
$[111]$	37° W+E	18° N+S	

From this data, the B 's are plotted on the stereographic projection, Figure 19(a). The following data were measured from the prints, where θ is the angle between g and \underline{u}_p :

g	θ	Sense of θ	
$[200]$	88°	CCW	
$[\bar{2}20]$	38°	CW	(B-9)
$[111]$	80°	CCW	

A standard $\langle 001 \rangle$ projection is constructed, and the B 's are plotted on it. Next, the \underline{u}_p 's are plotted from the data in Table (B-9). The great circles are drawn, and it

is seen from Figure 19(b) that the intersection of the great circles is $\{0\bar{1}1\}$, so $\underline{u} = \{0\bar{1}1\}$.

Determination of the Slip Plane

The slip plane is defined as $\underline{b} \times \underline{u}$, because the slip plane normal must be perpendicular to both \underline{b} and \underline{u} . For Dislocation A, $\underline{b} = a/2[101]$ and $\underline{u} = \{0\bar{1}1\}$, so the slip plane is:

$$[101] \times \{0\bar{1}1\} = (\bar{1}11) . \quad (B-10)$$

Therefore, the dislocation is characterized as $(\bar{1}11)a/2[101]$.

Determination of Fault Character

In the FCC lattice, two types of stacking faults commonly occur on $\{111\}$ planes. An intrinsic fault corresponds to a missing plane in the stacking sequence, while an extrinsic fault corresponds to an extra plane. The character of the fault can be determined by a number of methods [66], and two that were used in this study are now described.

The phase angle, α , between the transmitted and diffracted beams is [66]:

$$\alpha = 2\pi g \cdot \underline{R}_f . \quad (B-10)$$

The sign of the phase angle can be determined by the following procedure [66]: The fault is imaged in brightfield under two-beam conditions at a deviation parameter, w , equal to zero (Kikuchi band is centered between transmitted and diffracted beams). If the outermost fringes are light on a positive print, α is positive. If the outermost fringes are dark, α is negative. Since g is known, the sign of R_f can be determined. Intrinsic faults have $R_f = -1/3\langle 111 \rangle$, while extrinsic faults have $R_f = +1/3\langle 111 \rangle$.

For example, the large fault seen in Figure 17 is imaged at $w = 0$ and $g = [020]$. The direction of R_f was determined earlier in this appendix to be $[\bar{1}11]$. Since the outermost fringes are dark, $g \cdot R_f$ is negative. Therefore, R_f must be $-1/3[\bar{1}11]$, and the fault is intrinsic.

Another method for determining the nature of the fault was also used. A darkfield micrograph is taken at $w = 0$, and the g -vector is placed at the center of the fault. In thick crystals, absorption causes an asymmetry in the fringe pattern in darkfield, so one outer fringe is light while the other is dark. Under $\langle 200 \rangle$, $\langle 222 \rangle$, or $\langle 440 \rangle$ g -vectors, the g -vector points away from the light fringe in intrinsic faults, while it points toward the light fringe in extrinsic faults. As shown in Figure 17(b), the $\langle 200 \rangle$ g points away from the light fringe, thus confirming the intrinsic nature of the fault.

APPENDIX C
CALCULATION OF THE CRITICAL STRESSES
IN THE HUTHER-REPPICH MODEL

According to the Huther-Reppich model, the CRSS for a superalloy with overaged, spherical particles which are cut by strongly coupled dislocation pairs is given by Equation (2-7):

$$\Delta\tau_c = \{0.86 (Tf^{1/2}w)/(bd)\} \{1.28(d\gamma_o/wT) - 1\}^{1/2}, \quad (C-1)$$

where the terms are defined in the text. The stress to cause the first dislocation to penetrate the precipitate is given by Equation (2-8):

$$\Delta\tau_c = (\gamma_o/b) - (Gb/2r_s) . \quad (C-2)$$

Since by-pass did not occur at low temperatures, and since the two mechanisms are essentially in series, the largest of the two stresses predicted by Equations (C-1) and (C-2) will be the CRSS. The following values were measured for PWA 1480:

$$\begin{aligned} f &= 0.6 \\ b &= 2.5 \times 10^{-8} \text{ cm} \end{aligned}$$

$$d = 5 \times 10^{-5} \text{ cm}$$

The value of G can be estimated as G_{Ni} parallel to $\{111\}\langle 110 \rangle$, which is 57 GPa at 20°C [11]. The values of γ_0 and w have been estimated for similar alloys, and will be assumed to be close to the values for PWA 1480: The value of γ_0 for Mar-M 200 has been estimated to be 160 dynes/cm [11], and the value of w has been estimated to be 2.8 for Nimonic 105 by Reppich et.al [48].

Using the constant line tension approximation, the value of the shearing stress, Equation (C-1), is 230 MPa, while the value for the penetration stress, Equation (C-2), is 620 MPa. Even when G is varied between 50 and 80 GPa and γ_0 is varied between 100 and 200 dynes/cm, the shearing stress never exceeds 75% of the penetration stress. Thus, the penetration stress is always larger than the shearing stress, and the penetration stress controls the CRSS in the Huther-Reppich model.

The actual CRSS is about 400 MPa. This value is predicted more accurately by the Copley-Kear penetration stress, which resulted in a CRSS of 420 MPa for Mar-M 200 [11].

APPENDIX D
CALCULATION OF THE TRUE
ACTIVATION ENERGY FOR YIELDING

The apparent activation energy for yielding at high temperatures was calculated to be 50 kJ/mol by Equation (4-1). The true activation energy, which should be physically meaningful, may be derived in the following way: Since the deformation mechanisms which operated during tensile yielding and steady-state creep were the same, the yielding data may be correlated by a steady-state creep equation. However, this approach does involve some fundamental assumptions:

- i) The plastic strain rate is constant during yielding.
- ii) At high stresses and very high temperatures, primary creep (during yielding) may be ignored. OR
- iii) At high stresses and very high temperatures, the rate-limiting step during primary and steady-state creep is the same.

Although Assumptions (ii) and (iii) are speculative, some

supporting evidence is available. Several studies have shown that the primary creep strain produced in $\langle 001 \rangle$ oriented single crystal or D.S. superalloys is almost negligible at temperatures above about 850°C [9,27,29,68]. Also, in a study of In738 which was creep tested at various stress levels at 850°C , the primary creep strain was reduced from 1% at 200 MPa to almost zero at 400 MPa [29]. This indicates that primary creep may be negligible at the high stresses which develop during yielding. In support of Assumption (iii), several studies have shown that the deformation mechanism at high temperatures in alloys similar to PWA 1480 is the same during primary and steady-state creep [26,28]. Perhaps the strongest support for this argument lies in the similarity of the deformation substructures which developed during steady-state creep and yielding. On the other hand, creep data for PWA 1480 indicate that primary creep may not be negligible [69], and several studies have indicated that that the amount of primary creep strain is increased as the stress is increased [69,70]. Therefore, it appears that Assumption (iii) is the one which may most reasonably be invoked.

The steady-state creep rate is represented by [71]:

$$\dot{\epsilon}_s = A (\sigma/E)^n \exp(-Q_c/RT) , \quad (\text{D-1})$$

where σ = Applied stress,
 A, n = Material dependent constants,
 Q_c = Apparent activation energy for creep.

Under the assumptions outlined above, the activation energy for creep and yielding should be the same, and the yield stress can be substituted for the creep stress. The resulting equation for the yield stress is:

$$\ln(\sigma/E) = (Q'/Rn)(1/T) + \{\ln(\dot{\epsilon}_g/A)\}/n. \quad (D-2)$$

From Equations (4-1) and (D-2) the true activation energy for yielding, Q_y , can be calculated from the apparent activation energy for yielding, Q' :

$$Q_y = n \cdot Q', \quad (D-3)$$

where n is the stress exponent in Equation (D-1). From published creep data on PWA 1480 at 871°C [72], the stress exponent has a value of about 10, which is within the range of values for similar alloys [27-29,73,74]. By Equation (D-3), the true activation energy for yielding is calculated to be 500 kJ/mol, which is well within the range of apparent activation energies for steady-state creep in similar alloys [26,28,29,73,75].

By using the effective stress approach, it has been

demonstrated that the true activation energy for creep in these alloys is very close to the activation energy for self-diffusion. This indicates that the rate-limiting step in creep deformation in these alloys is diffusion-controlled. Since the activation energy for yielding in PWA 1480 was in the range of apparent creep activation energies for similar alloys, it appears that the yielding process in PWA 1480 at high temperatures was diffusion controlled as well.

Table 1 - Alloy Composition

Element	Weight Percent
Al	4.8
Ti	1.3
Ta	11.9
Cr	10.4
Co	5.3
W	4.1
C	(42 ppm)
Ni	Bal.

Table 2 - Test Data

Sample #	Temperature (°C)	Strain Rate (%/min)	Degrees From <001>	Elastic Modulus (GPa)	Plastic Strain (%)	Offset Yield Strength (MPa)		
						0.05%	0.1%	0.2%
61-2	20	0.5	6	137	0.14	1010	1015	---
37-2			4	120	0.24	1006	1020	1034
70-1	705	0.5	3	105	0.08	970	---	---
35-2			6	105	0.29	1000	---	---
70-2		50	3	105	0.14	970	1034	1120
35-1			6	103	0.35	950	1000	---
60-1	760	0.5	5	100	0.11	844	970	1034
44-2			10	103	0.26	893	---	---
60-2		50	5	96	0.14	908	956	1048
44-1			10	105	0.35	950	1000	---
1-1	815	0.5	6	94	0.10	949	978	1062
83-1			5	94	0.25	675	696	---
1-2		50	6	98	0.19	640	683	774
83-2			5	98	0.34	942	1006	---
5-1	871	0.5	4	94	0.09	886	957	1083
40-2			8	92	0.24	535	---	---
5-2		50	4	95	0.15	506	549	612
40-1			8	102	0.32	788	823	---
42-1	927	0.5	4	86	0.09	816	865	932
39-1			6	87	0.24	373	---	---
42-2		50	4	90	0.18	394	422	457
39-2			6	94	0.35	640	682	---
7-1	982	0.5	6	91	0.10	675	710	767
63-1			5	81	0.25	302	323	---
7-2		50	6	88	0.19	299	309	351
63-2			5	80	0.34	510	538	---
2-1	1093	0.5	5	71	0.09	492	527	583
37-1			4	71	0.22	168	---	---
2-2		50	5	72	0.20	172	183	221
61-1			6	77	0.38	274	295	310
						302	316	330

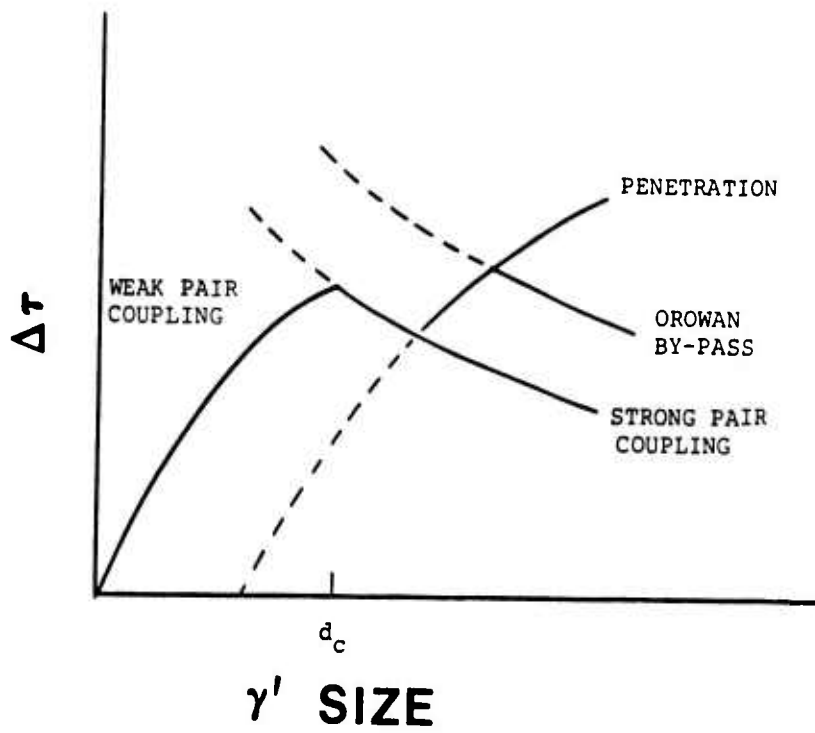
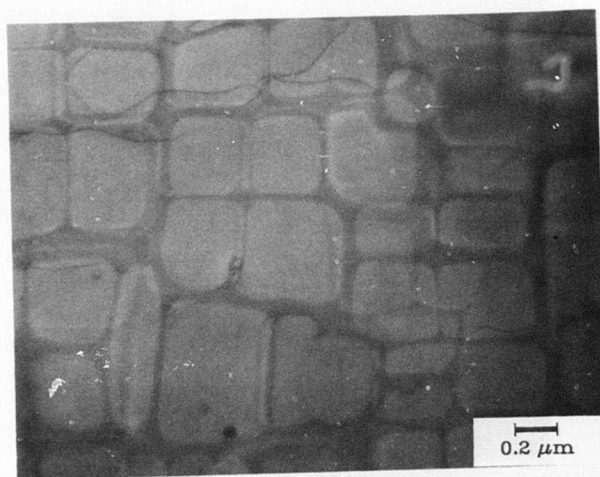
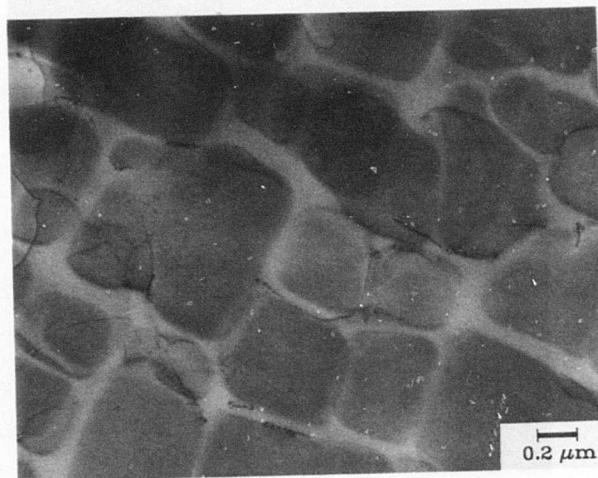


Fig 1. CRSS vs Particle Size for a 50 v/o γ/γ' alloy according to Huther-Reppich model [45].

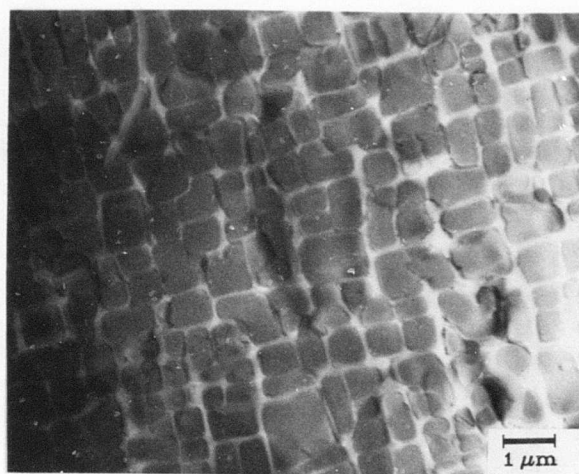


(a)

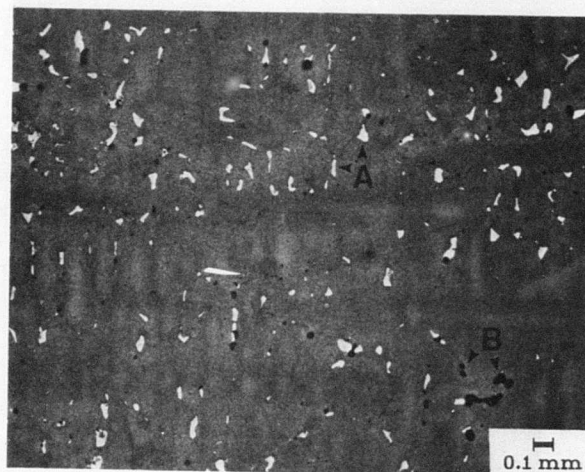


(b)

Fig 2. TEM micrographs illustrating electropolishing behavior. (a) 8.5 V, γ' attacked. (b) 10.0 V, matrix attacked.



(a)



(b)

Fig 3. Initial microstructure. (a) Brightfield TEM micrograph of the γ/γ' structure, $g = \langle 200 \rangle$. (b) Optical micrograph showing residual dendritic structure, eutectic areas (A), and micropores (B).

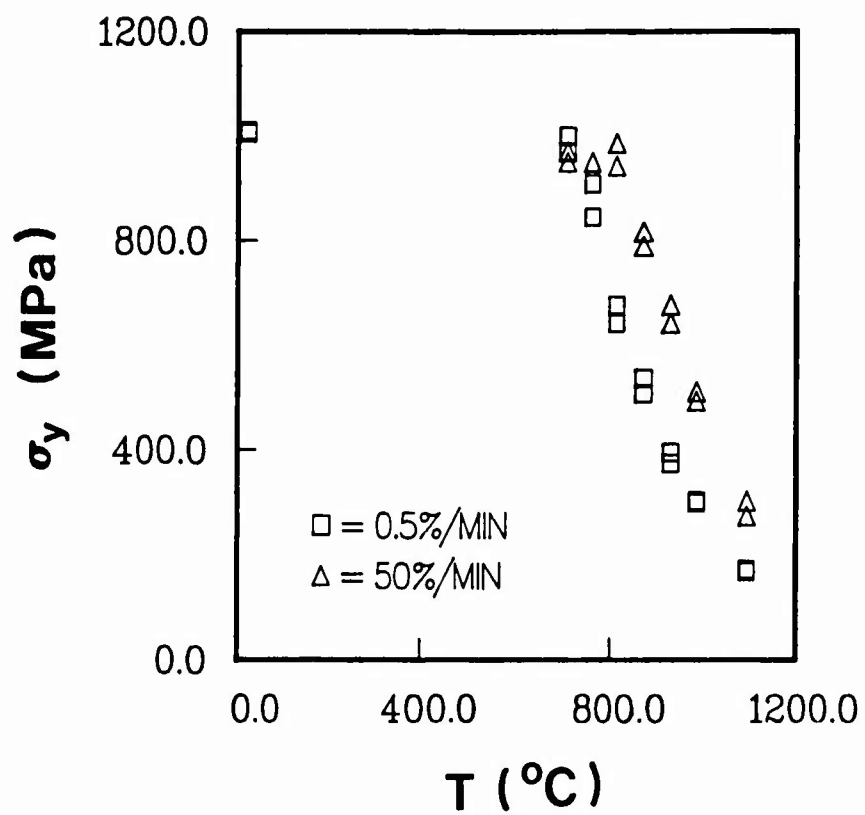


Fig 4. Yield Strength at 0.05% offset vs Temperature.

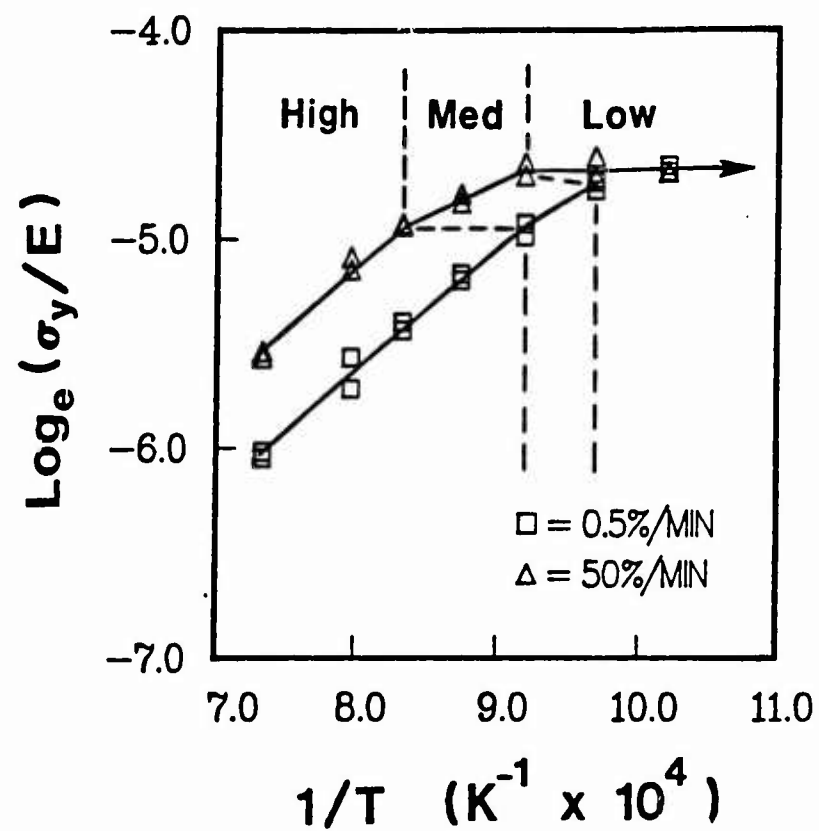
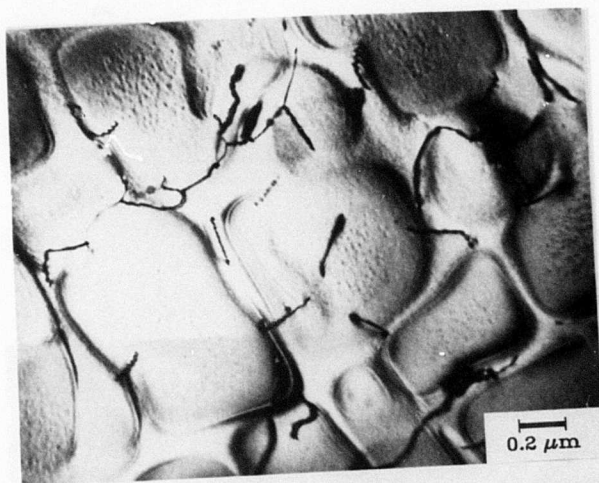


Fig 5. Arrhenius representation of the 0.05% Yield Strength data. Slopes were determined by least-squares analysis.



(a)



(b)

Fig 6. Typical low temperature deformation structures.
 (a) #61-2, 20°C, $\epsilon_p = 0.14\%$, $\langle 001 \rangle$ Zone Axis
 multibeam condition. (b) #70-2, 705°C, $\epsilon_p = 0.14\%$,
 $\langle 001 \rangle$ Zone Axis multibeam condition.

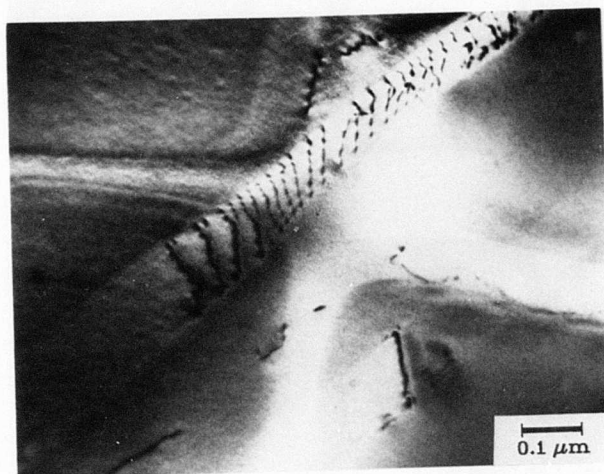
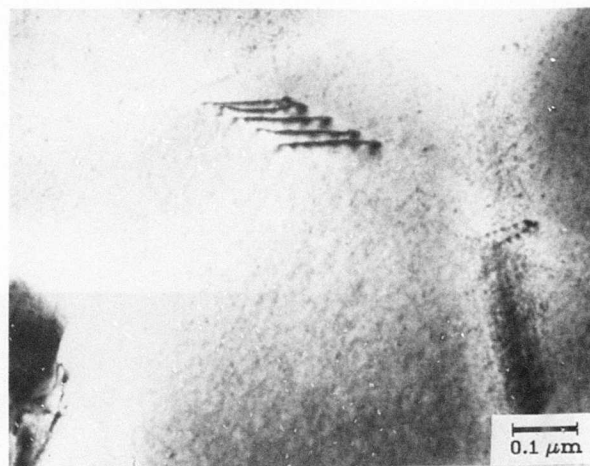
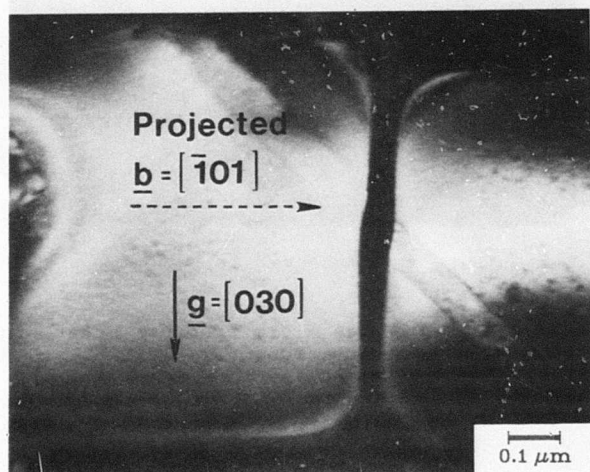


Fig 7. Micrograph showing splitting of $a/2\langle 110 \rangle$ pairs upon emerging from the precipitate. #70-1, 705°C , $\epsilon_p = 0.08\%$, $g = \langle 200 \rangle$.



(a)



(b)

Fig 8. Shearing of γ' in #70-1. (a) Bright field, $g = [\bar{1}11]$. (b) Superlattice dark field of same area, $g = [030]$. The Burgers vector, $a/2[\bar{1}01]$, is at a 45° angle to the micrograph. Dislocations are invisible in (b) because $g \cdot \underline{b} = 0$.

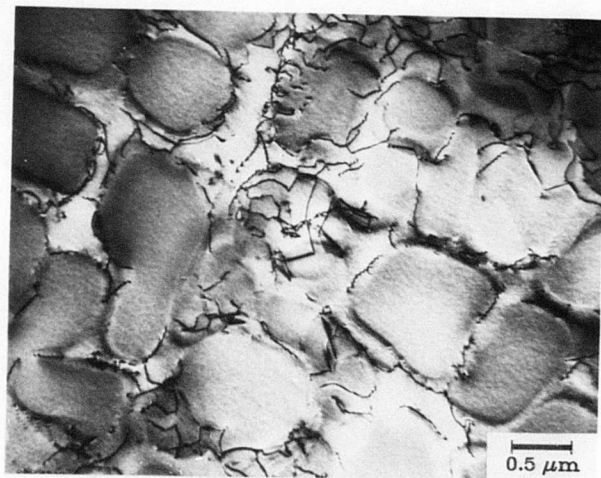


Fig 9. Typical γ' by-pass microstructure after high temperature deformation. #63-1, 982°C, $\epsilon_p = 0.25\%$, $g = \langle 200 \rangle$.

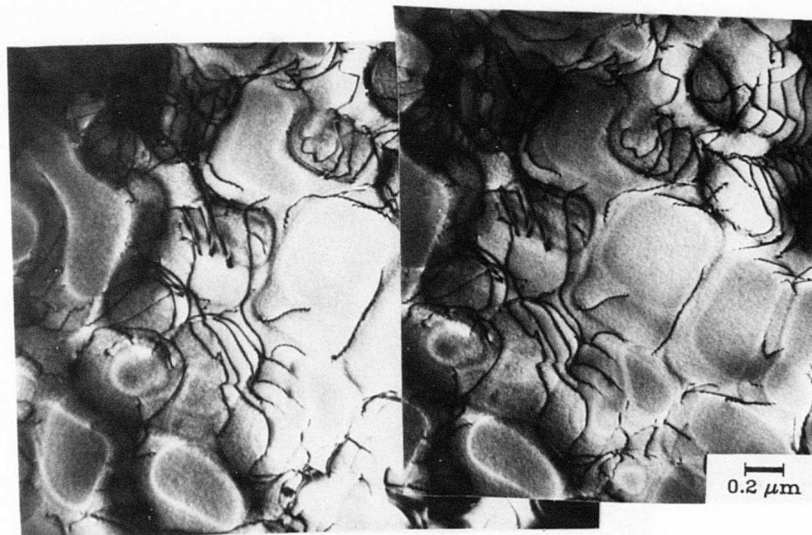


Fig 10. Stereo pair showing dislocations wrapping around the γ' precipitates. #7-1, 982°C, $\epsilon_p = 0.10\%$, $g = \langle 111 \rangle$.

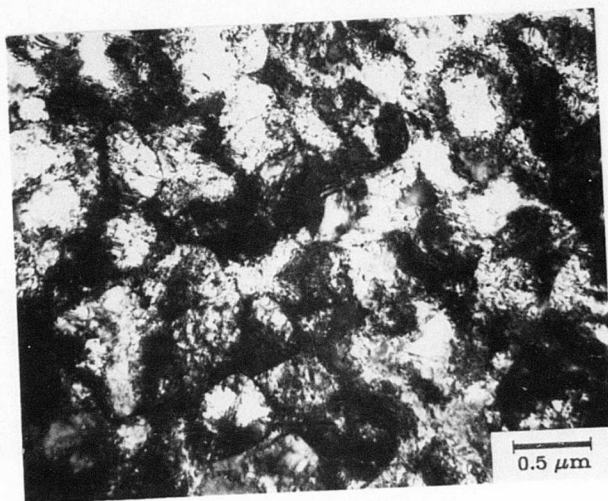
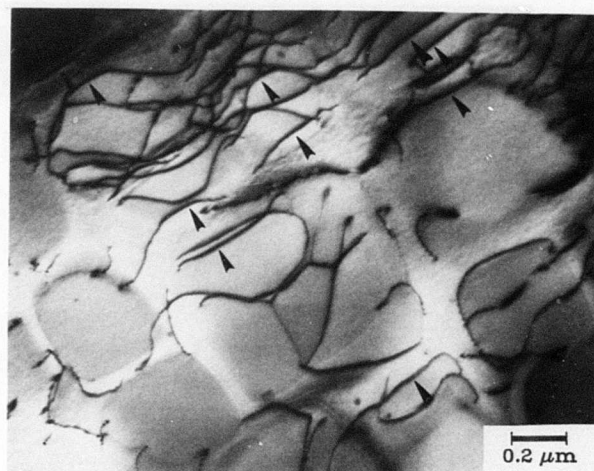
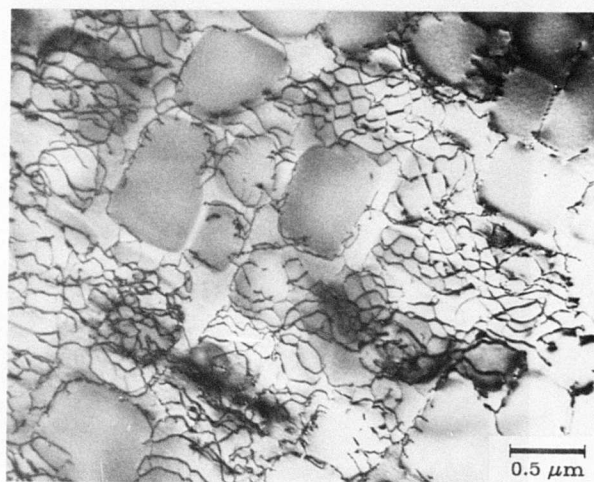


Fig 11. High dislocation density after testing to failure
at 871°C at the slow strain rate. #JA36, $g = \langle 111 \rangle$.

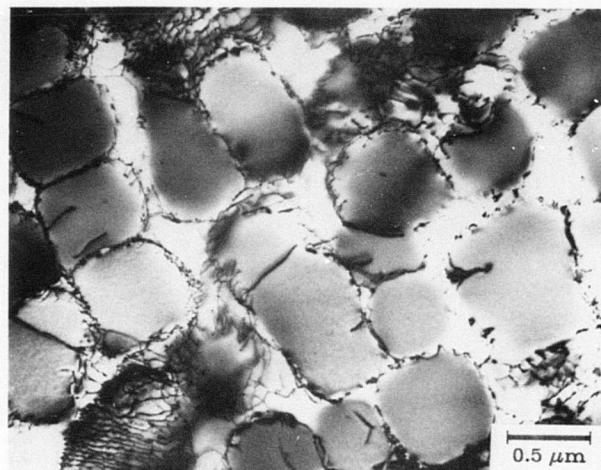


(a)

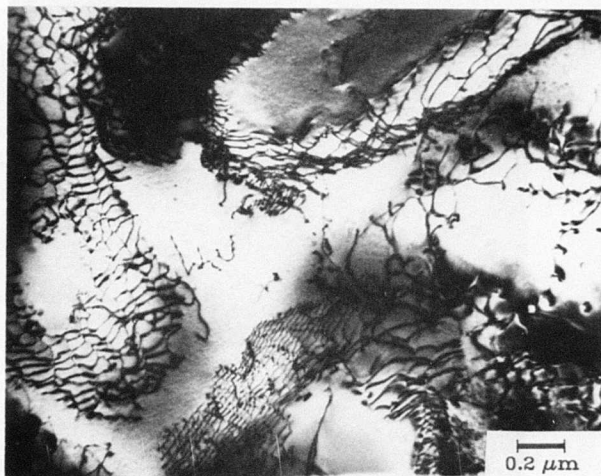


(b)

Fig 12. Interfacial arrays developed at very high temperatures. (a) Marked segments cross-slipped to $\{011\}$ at low strains. #2-1, $\epsilon_p = 0.09\%$, $g = \langle 200 \rangle$. (b) Arrays developed at higher strains. #37-1, $\epsilon_p = 0.22\%$, $g = \langle 200 \rangle$.

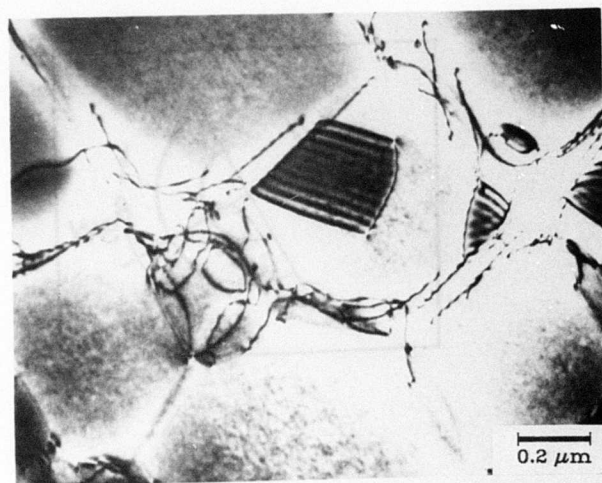


(a)

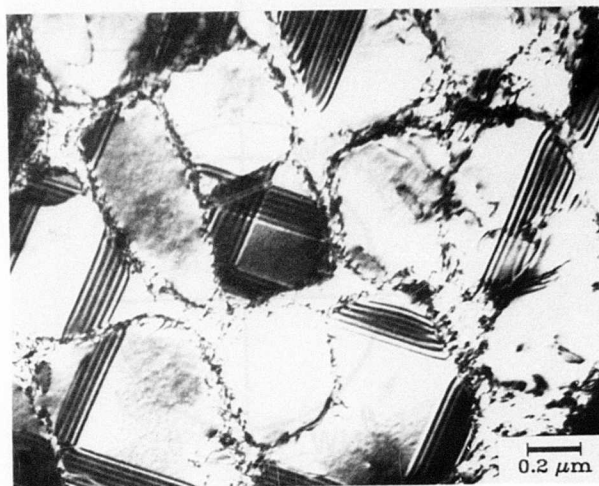


(b)

Fig 13. Substructures after failure at 1093°C.
 (a) Tensile test, #JA38, 0.5%/min, $g = \langle 200 \rangle$.
 (b) Creep test, #JA48, $\sigma = 117$ MPa, $g = \langle 220 \rangle$.
 Note coarsening of γ' .

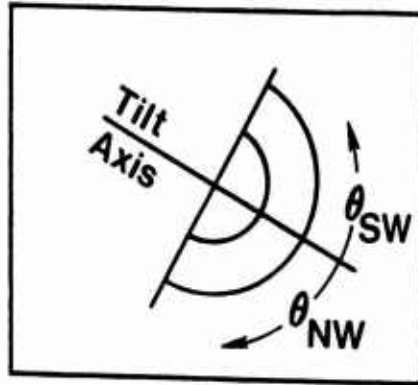


(a)

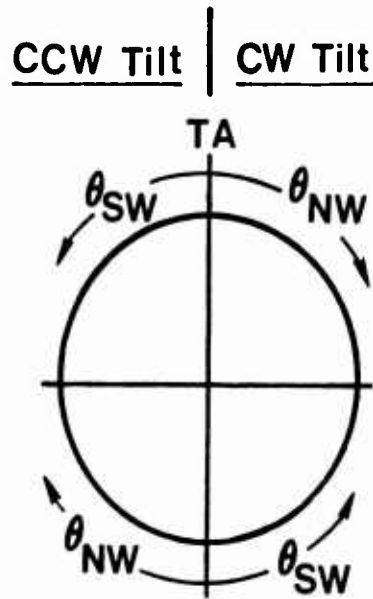


(b)

Fig 14. Shearing by the $\{111\}\langle 112 \rangle$ system at 760°C and slow strain rate. (a) #44-2, $\epsilon_p = 0.26\%$, $g = \langle 111 \rangle$, $w = 0.1$. (b) #JA34, tested to failure (14% elongation), $g = \langle 200 \rangle$, $w = 0$.



(a)



(b)

Fig 15. (a) TEM screen with tilt axis labelled. (b) Wulff net set-up relative to TEM screen.

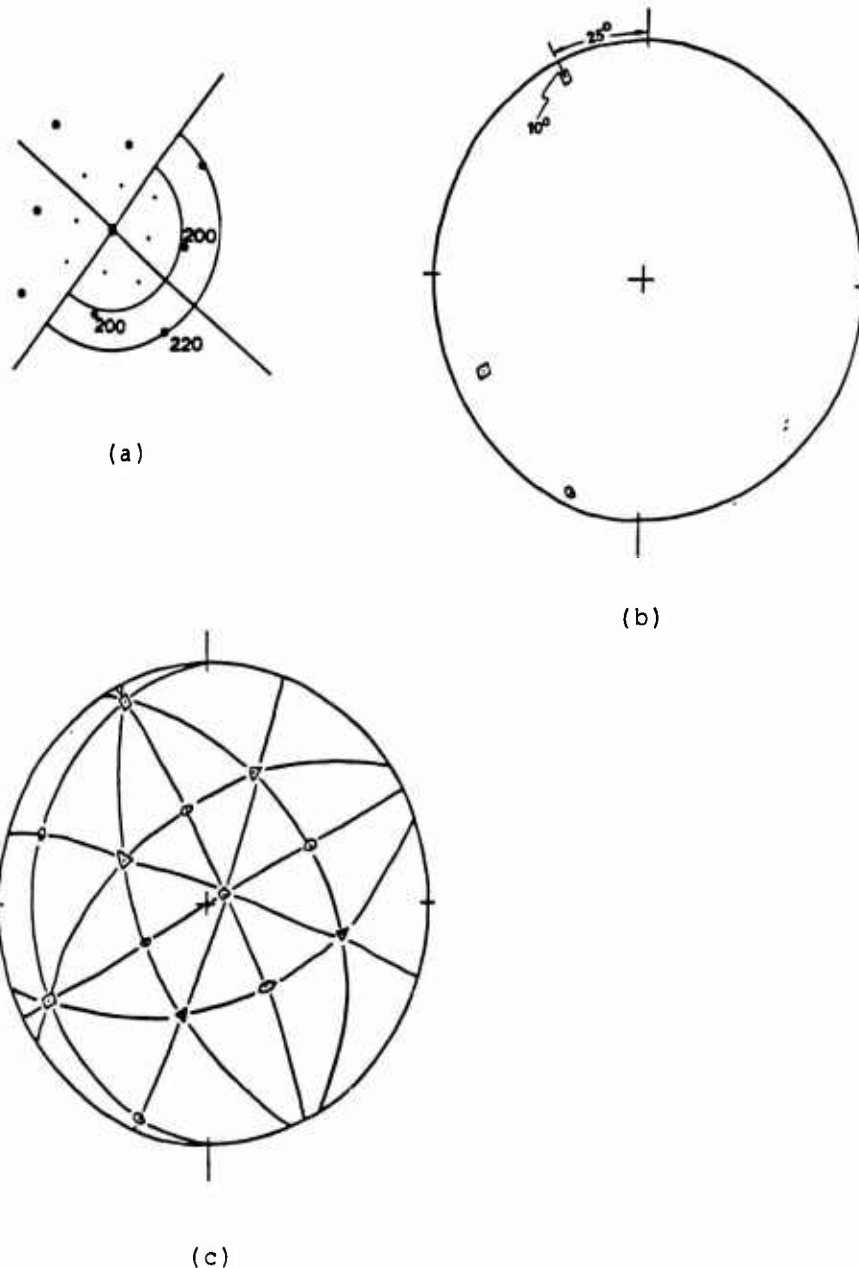


Fig 16. Determination of crystal orientation.
 (a) Diffraction pattern in TEM. (b) Plotting of the first $\langle 200 \rangle$ pole (Appendix A). (c) Final stereographic projection.

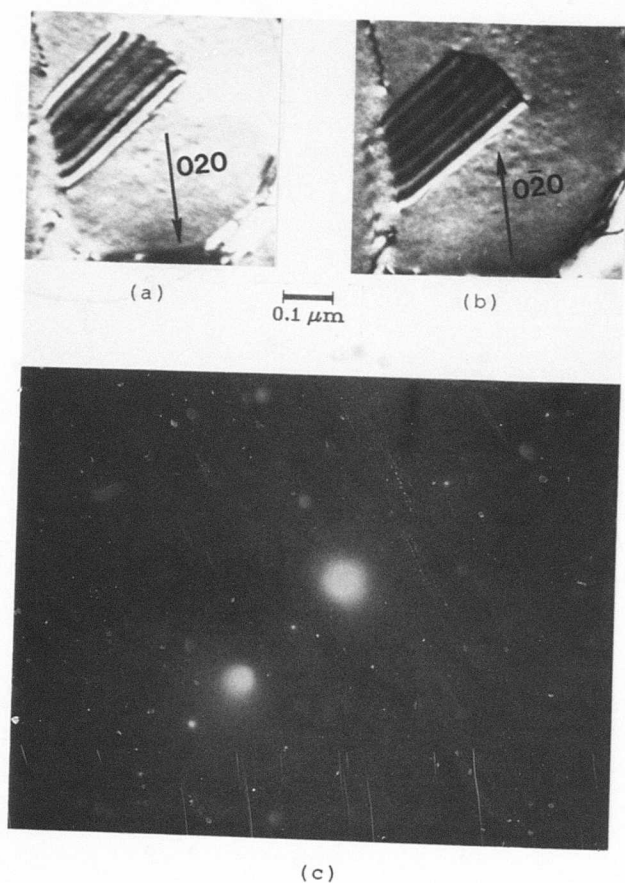


Fig 17. (a) Brightfield micrograph of a stacking fault at $g = \langle 200 \rangle$ and $w = 0$. (b) Darkfield micrograph under same conditions. (c) Selected area diffraction pattern.

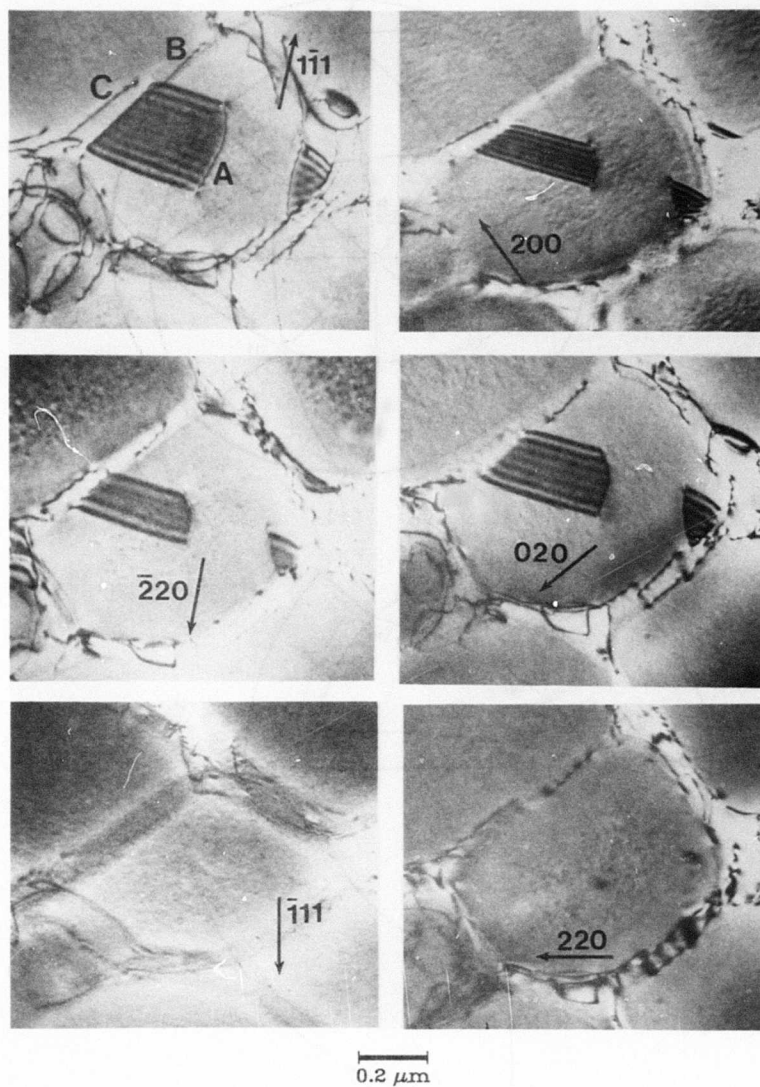
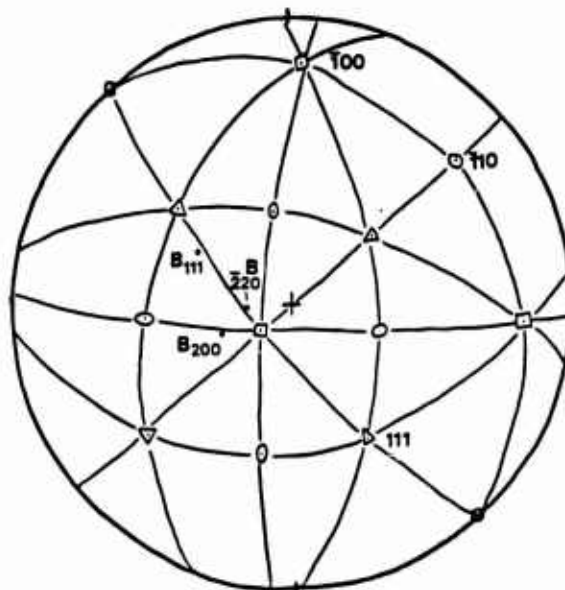
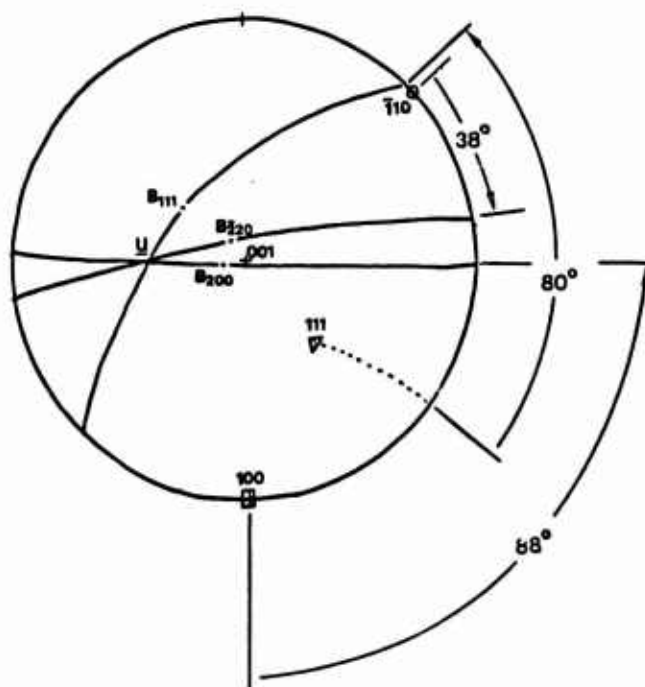


Fig 18. Dislocation analysis. (See Appendix B).



(a)



(b)

Fig 19. Line direction determination. (See Appendix B).

1. Report No. NASA CR 175100 USAAVSCOM TR 86 C-18		2. Government Accession No.		3. Recipient's Catalog No.	
4. Title and Subtitle Yielding and Deformation Behavior of the Single Crystal Nickel-Base Superalloy PWA 1480				5. Report Date May 1986	
				6. Performing Organization Code	
7. Author(s) Walter W. Milligan, Jr.				8. Performing Organization Report No. None	
				10. Work Unit No.	
9. Performing Organization Name and Address Georgia Institute of Technology School of Materials Engineering Atlanta, Georgia 30332-0245				11. Contract or Grant No. NAG 3 503	
				13. Type of Report and Period Covered Contractor Report	
12. Sponsoring Agency Name and Address U.S. Army Aviation Research and Technology Activity - (AVSCOM), Propulsion Directorate, Lewis Research Center, Cleveland, Ohio 44135 and NASA Lewis Research Center, Cleveland, Ohio 44135				14. Sponsoring Agency Code 533-13-00	
15. Supplementary Notes Intermediate report. Project Managers: Robert C. Bill, Propulsion Directorate, U.S. Army Aviation Research and Technology Activity - AVSCOM; Rebecca A. MacKay, Materials Division, NASA Lewis Research Center. This report was a thesis submitted in partial fulfillment of the requirements for the degree Master of Science in Metallurgy to Georgia Institute of Technology, Atlanta, Georgia in March 1986.					
16. Abstract <i>Gamma Prime</i> Interrupted tensile tests were conducted to fixed plastic strain levels in <001> oriented single crystals of the nickel-base superalloys PWA 1480. Testing was done in the range from 20-1093°C, at strain rates of 0.5 and 50%/min. The yield strength was constant from 20-760°C, above which the strength dropped rapidly and became a strong function of strain rate. The high temperature data could be represented very well by an Arrhenius-type equation, which resulted in three distinct temperature regimes. The deformation substructures could be grouped in the same three regimes, indicating that there was a fundamental relationship between the deformation mechanisms and activation energies. At low temperatures, the activation energy for yielding was zero, and deformation occurred by γ' shearing by pairs of $a/2\langle 110 \rangle$ dislocations on octahedral planes. At high temperatures, the true activation energy for yielding was indicative of a diffusion-controlled process, and deformation occurred by γ' by-pass. Intermediate temperatures exhibited transitional behavior. Models of the yielding process were considered, and it was found that no currently available model was fully applicable to this alloy. It was also demonstrated that the initial deformation mechanism (during yielding) was frequently different from that which would be inferred by examining specimens which had been tested to failure.					
17. Key Words (Suggested by Author(s)) Nickel-base superalloy; Precipitation hardening; Single crystal; Deformation mechanisms				18. Distribution Statement Unclassified - unlimited STAR Category 26	
19. Security Classif. (of this report) Unclassified		20. Security Classif. (of this page) Unclassified		21. No. of pages	
				22. Price*	